Chapter 2

Metal-organic hybrids based on a $[VO_2(L)]$-tecton with cations of imidazole derivatives: Synthesis, characterization and *in vitro* antidiabetic activity

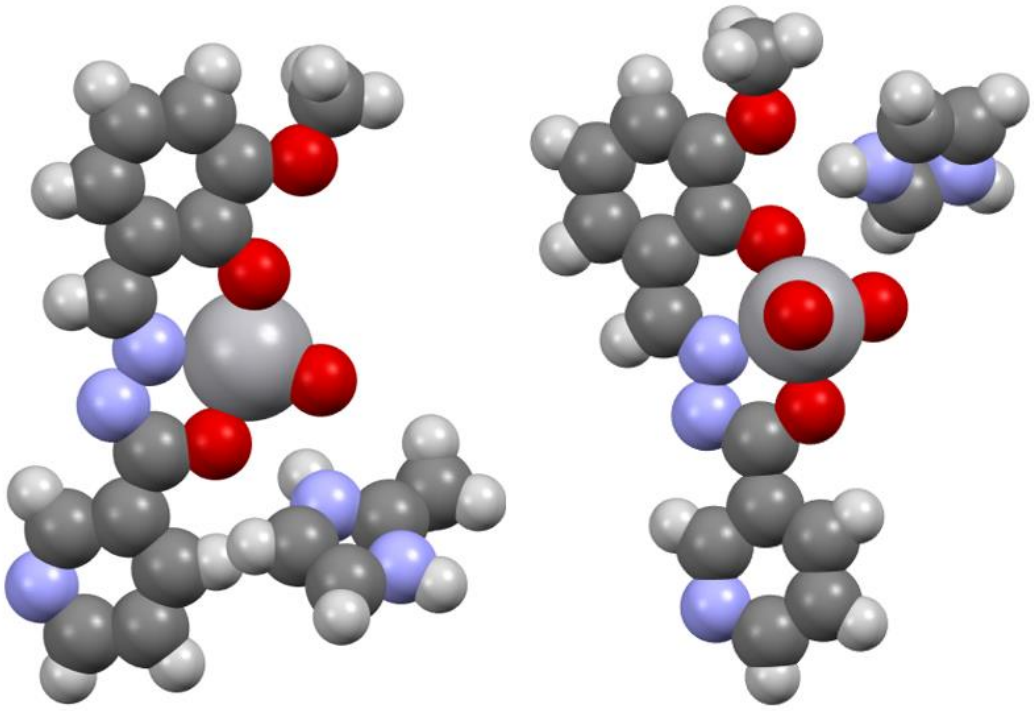

1 Introduction

Nowadays metal-organic hybrids are an outstanding topic and dynamic area of research because of their fascinating architectures and topologies [1-8]. It has been found that such compounds are very useful due to their potential application in catalysis [9-11], separation process [12-14], gas storage [15-17], magnetism [18-20] and sensors [21-22]. Such metal-organic hybrids can be manufactured by a covalent path using potentially tridentate ligands or by a non-covalent path using hydrogen bondings and other weak interactions.

The covalent path is based on strong coordinate bonds connecting the cations and organic ligands into vigorous polymeric structures. In the non-covalent path very weak non-covalent forces like hydrogen bonding, C-H···π interactions, π···π stacking and halogen bondings are used. Among the non-covalent interactions, hydrogen bonding is an especially strong building motif used in crystal engineering as it yields unique directionality and can be very easily inserted into structures.

For the construction of desired framework and functionality in synthetic compounds, it is important to control and find out factors such as counterions, solvents, temperature and pH-value that suggest influencing the structural prediction on the assembly on the final coordination framework and controlling the crystal growth and the stability of crystals [23]. Among the above factors, counter ions have an important effect on the formation of compounds. Different coordination abilities, sizes and geometries of cation have a significant influence on the crystal structures of coordination compounds [24]. Hydrated cations of imidazole and its derivatives are useful tectons due to their different size and charge especially hydrogen bonding ability led to the formation of a high-dimensional framework [25]. Recently, the use of bioactive metal-organic framework (BioMoFs) has gained significant attention in medical science. Vanadium complexes possess various biological roles in living organisms [26-28] and are considered suitable candidates in the search for new orally active chemotherapeutics as an alternative for the existing antidiabetic drugs. Because of above efforts, the syntheses of new vanadium complexes with high bio-availability and low toxicity have synthesized new dioxidovanadium complexes with potentially tridentate ONO donor Nicotinic acid (2-hydroxy-3-methoxy-benzylidene)-hydrazide (H_2L) ligand and imidazole derivatives (Imidazole, 2-methylimidazole, 1-methylimidazole, 2-ethylimidazole, benzimidazole and 2-methyl benzimidazole). However, to the best of our knowledge $[VO_2(L)]^-$ tecton with above-substituted imidazoles and their insulin-mimetic activity studies

are not yet designed and reported. Structural characterizations of six new complexes were carried out by elemental and different spectral techniques. The insulin-mimetic activity of these complexes has also been explored and compared with similar complexes.

2 Experimental

2.1 Materials

All chemicals for syntheses were purchased commercially and were used without further purification. Vanadium pentaoxide was purchased from Across Organics. Spectroscopic grade solvents are used for spectroscopic and electrochemical measurements.

2.2 Physical Measurements

The C, H and N contents of compounds were obtained on a Euro Vector EA3000 elemental analyzer. FTIR spectra were measured with a KBr pellet on a Bruker alpha FTIR-Spectrophotometer at 298 K. NMR spectrum of ligand was recorded on a Bruker Advance III 400MHz spectrometer. ESI Mass spectrometry was recorded on a XEVO G2-XS QTOF. UV-visible spectra were recorded on a Shimadzu UV-1601 Spectrophotometer. Cyclic voltammetry (CV) experiments were carried out on a BAS-100 electrochemical analyzer in 3×10^{-3} M DMSO solutions. A three-electrode setup was employed consisting of a glassy carbon working electrode, a platinum auxiliary electrode and Ag/AgCl as reference electrode 0.1 M. tetra butyl ammonium perchlorate (TBAP) was used as supporting electrolyte. The ferrocenium/ferrocene couple was used to measure the redox potential. All measurements were done at 298K under a nitrogen atmosphere. TGA analysis has been carried out in the Shimadzu DTG-60 automatic thermal analyzer instrument in the temperature range of 25-550 °C with a heating rate of 10 °C min^{-1}. Single crystal X-ray diffraction data of complexes were collected at room temperature on X'calibur CCD area-detector diffractometer equipped with graphite monochromatic MoKα radiation (λ = 0.71073 Å). The crystal used for data collection was of suitable dimensions. The unit cell parameters were determined by least-square refinements of all reflections in both cases. All the structures were solved by direct technique and refined by full-matrix least-square on F2. Data were corrected for Lorentz, polarization and multi-scan absorption correction [29]. All structures were solved by direct methods using SHELXS97 [30]. All non-hydrogen atoms were located in the best E-map. Full-matrix least-squares refinement was carried with SHELXL97 [30]. The geometry of the molecule has been calculated using the software PLATON [31] and PARST [32].

Tetracyanoethylene (TCNE) was used as a field marker (g = 2.00277). NMR spectra were carried out on a Bruker 300/400.

2.3. Synthesis

2.3.1 Synthesis of Schiff base (H_2L)

Nicotinic acid hydrazide (1.371 g, 10 mmol) and ortho-vanillin (1.521 g, 10 mmol) were mixed to an ethanol (100 mL) and refluxed for 3 hrs at 80°C. After refluxing the orange solution was cooled to room temperature and the resulting precipitate was filtered and washed with cold ethanol and stored in a $CaCl_2$ desiccator.

M.P.: 180 °C. Yield: 87%. Anal. Calc. for $C_{14}H_{13}N_3O_3$ (271.27 g mol^{-1}): C, 61.98; H, 4.83; N, 15.49%; Found: C, 61.96; H, 4.85; N, 15.51%. FTIR bands (KBr, cm^{-1}): ν(O–H) 3544 m, ν(N–H) 3368 w, ν(C=N) 1672 m. ^{1}H NMR (DMSO-d_6, 400 MHz) δ: 12.2 (s, 1H, Ar-OH), 10.8 (s, 1H, –NH), 8.7 (s, 1H, –CH=N-), 6.8-9.0 (m, 7H, Ar-H), 3.82 (s, 3H, -OCH_3), ppm. ^{13}C-NMR (DMSO-d_6, 400 MHz) δ: 161 (C=O), 152 (C=N), 114-148 (Ar-C), 56 (-OCH_3) ppm.

2.3.2 Synthesis of $[VO_2(L)]$ImH 1

10 mL methanolic solution of vanadium pentaoxide (0.188 g, 1 mmol) was added dropwise to a 10 mL methanolic solution of HL (0.271 g, 1 mmol) at ambient temperature. To this reaction mixture (0.068 g, 1 mmol) ImH (imidazole) was added. The reaction mixture was refluxed for 3 hrs at 80°C, cooled to room temperature. The reaction mixture was allowed to evaporate slowly in the air. After one-week brown crystals of **1** separated, which were collected upon filtration and dried in a $CaCl_2$ desiccator.

Yield: 97%. Anal. Calc. for $C_{17}H_{16}N_5O_5V$ (421.29 g mol^{-1}): C, 48.46; H, 3.82; N, 16.62%; Found: C, 48.49; H, 3.85; N, 16.58%. FTIR bands (KBr, cm^{-1}): ν(C=N) 1672 (m), ν(C-O) 1223 (vs), ν(V=O) 951 (s), ν(V-O) 465 (m), ν(V-N) 424 (vs) cm^{-1}. ESI Mass (m/z) = 422.09.

2.3.3 Synthesis of $[VO_2(L)]$2-MeImH 2

10 mL methanolic solution of vanadium pentoxide (0.188 g, 1 mmol) was added dropwise to a 10 mL methanolic solution of HL (0.271 g, 1 mmol) at ambient temperature.

To this reaction mixture2-MeImH (2-methylimidazole) (0.082 g, 1 mmol) was added. The reaction mixture was refluxed for 3 hrs at 80°C, cooled to room temperature. The reaction mixture was allowed to evaporate slowly in the air. After one-week brown crystals of **1** separated, which were collected upon filtration and dried in $CaCl_2$ desiccator.

Yield: 61%. Anal. Calc. for $C_{18}H_{18}N_5O_5V$ (435.31 g mol^{-1}): C, 49.66; H, 4.16; N, 16.08%; Found; C, 49.62; H, 4.14; N, 16.09%. FTIR bands (KBr, cm^{-1}): ν(C=N) 1635 (m), ν(C-O) 1248 (vs), ν(V=O) 967 (s), ν(V-O) 465 (m), ν(V-N) 424 (vs) cm^{-1}. ESI Mass (m/z) = 436.32.

2.3.4 Synthesis of $[VO_2(L)]$M-ImH 3

To a suspension of H_2L (0.271 g, 1 mmol) in a methanol solution (20 mL) vanadium pentaoxide (0.188 g, 1 mmol) in methanol (10 mL) was added while stirring. To this reaction mixture M-ImH (1-methylimidazole) (0.082 g, 1 mmol) was added while stirring. The resulting solution was refluxed for 3 hrs at 80°C, cooled at room temperature and filtered. The filtrate was left to evaporate slowly in the air. After one weak yellow polycrystalline powder of **1** separated, which was collected upon filtration, washed with methanol and dried in $CaCl_2$ desiccator.

Yield: 71%. Anal. Calc. for $C_{18}H_{18}N_5O_5V$ (435.31 g mol^{-1}) C, 49.66; H, 4.40; N, 16.05%; Found: C, 49.62; H, 4.38; N, 16.08%. FTIR bands (KBr, cm^{-1}): ν(C=N) 1623 (m), ν(C-O) 1254 (vs), ν(V=O) 965 (s), ν(V-O) 474 (m), ν(V-N) 436 (vs) cm^{-1}. ESI Mass (m/z) = 436.08.

2.3.5 Synthesis of $[VO_2(L)]$2-EthImH 4

To a suspension of H_2L (0.271 g, 1 mmol) in methanol, obtained after stirring, was added 10 mL methanolic solution of vanadium pentaoxide (0.188 g, 1 mmol). To this reaction mixture 2-EthImH (2-ethylimidazole) (0.082 g, 1 mmol) was added while stirring. The resulting solution was refluxed for 3 hrs at 80°C, cooled to room temperature and filtered. The filtrate was allowed to evaporate in the open air. After 3-4 days, the light-yellow microcrystalline powder was isolated, washed with cold methanol and kept in a $CaCl_2$ desiccator.

Yield: 87%. Anal. Calc. for $C_{19}H_{20}N_5O_5V$ (449.34 g mol^{-1}) C, 50.79; H, 4.49; N, 15.59%; Found: C, 50.75; H, 4.47; N, 15.56%. FTIR bands (KBr, cm^{-1}): ν(C=N) 1632 (m),

ν(C-O) 1250 (vs), ν(V=O) 942 (s), ν(V-O) 459 (m), ν(V-N) 410 (vs) cm^{-1}. ESI Mass (m/z) = 450.50.

2.3.6 Synthesis of $[VO_2(L)]$BenzImH 5

To H_2L (0.271 g, 1 mmol) dissolved in 20 mL methanol to get suspension after stirring. In the suspension of H_2L 10 mL, a methanolic solution of vanadium pentaoxide (0.188 g, 1 mmol) was added and stirred for 30 min. To this stirred solution 10 mL of BenzImH (benzimidazole) (0.118 g, 1 mmol) was added and the resulting solution was refluxed for 3 hrs at 80°C, and cooled to room temperature and filtered. Finally, the solution was filtered and the filtrate was left overnight to slowly evaporate. The yellow-coloured microcrystalline powder was obtained which was washed with cold methanol and stored in a $CaCl_2$ desiccator.

Yield: 95%. Anal. Calc. for $C_{21}H_{18}N_5O_5V$ (471.08 g mol^{-1}) C, 53.51; H, 3.85; N, 14.86%; Found: C, 53.48; H, 3.87; N, 14.82%. FTIR bands (KBr, cm^{-1}): ν(C=N) 1633 (m), ν(C-O) 1281 (vs), ν(V=O) 950 (s), ν(V-O) 459 (m), ν(V-N) 425 (vs) cm^{-1}. ESI Mass (m/z) = 472.11.

2.3.7 Synthesis of $[VO_2(L)]$2-MeBenzImH 6

A 20 mL methanolic solution of H_2L (0.271 g, 1 mmol) was stirred for 10 min. to get a suspension of H_2L. To this suspension, a 10 mL methanolic solution of vanadium pentaoxide (0.188 g, 1 mmol) was added dropwise while stirring. To the yellow solution, 10 mL 2-MeBenzImH (2-methyl benzimidazole) (0.132 g. 1 mmol) was added and refluxed for 3 hrs at 80°C. The stirred solution was cooled to room temperature, filtered and the filtrate was left for slow evaporation at room temperature for a weak and polycrystalline yellow compound was obtained washed with methanol and stored under room temperature in a $CaCl_2$ desiccator.

Yield: 90%. Anal. Calc. for $C_{22}H_{20}N_5O_5V$ (485.37 g mol^{-1}) C, 54.44; H, 4.15; N, 14.43%; Found: C, 54.41; H, 4.17; N, 14.40%. FTIR bands (KBr, cm^{-1}): ν(C=N) 1633 (m), ν(C-O) 1280 (vs), ν(V=O) 947 (s), ν(V-O) 470 (m), ν(V-N) 442 (vs) cm^{-1}. ESI Mass (m/z) = 486.19.

2.4 Antidiabetic activity

2.4.1 Antioxidant activity

The 2,2-diphenyl-1-picrylhydrazyl (DPPH) radical scavenging activity of ligand and complexes **1** and **2** was determined following the method described by Datta et al [33] with slight modification. In brief, a 96-well, 50 µL of various dilutions (10-100 µg/mL) of methanolic extract 125 µL of tris–HCl buffer (0.1M, pH 7.4) and 125 µL of DPPH solution (0.004% w/v in methanol) were added. The reaction mixture was shaken well and incubated at 25 ℃ for 30 min. The DPPH decolorization was recorded at 518 nm on a BioTek Synergy H4 hybrid multimode reader (BioTek Instruments, Inc Winooski, VT, USA.). The percentage inhibition rate using the formula:

$$\text{DPPH scavenging activity (\%)} = [(A_C\text{-}A_S)/A_C \times 100]$$

where A_C is the absorbance of the control and A_S is the absorbance of samples Ascorbic acid was used as the positive control.

2.4.2 α-Glucosidase inhibition activity

The α-glucosidase inhibitory activity assay was investigated based on the reported in the literature, with a few modifications [34]. In brief, Rat-intestinal acetone powder was dissolved in 100 mL of saline water and sonicated properly at 4°C. After sonication, the suspension was centrifuged (3,000 rpm, 4°C, 30 minutes) and the resulting supernatant was used for the assay. A reaction mixture containing 50 µL of phosphate buffer (50 mM; pH 6.8), 50 µL of rat α-glucosidase and 50 µL sample of varying concentrations (100-800 µg/mL) was pre-incubated for 5 min at 37 °C and then 50 µL of 3 mM pNPG was added to the mixture as a substrate. After incubation at 37 °C for 30 min, enzymatic activity was quantified by measuring the absorbance at 405 nm in a microtiter plate reader (Bio-TEK, USA) and the values were compared with acarbose used as control. The α-glucosidase inhibitory activity (%) was calculated using the formula:

$$\text{\% inhibition} = [(A_C\text{-}A_S)/A_C] \times 100$$

where A_C and A_S are the absorbance changes of control and samples respectively. The inhibiter concentration in the reaction mixture required to inhibit 50% of the enzyme is known as IC_{50}.

2.4.3 α-Amylase inhibition activity

Pancreatic α-amylase assay was adopted using the procedure described by Sudha et al. [35] Briefly 50 µL of different dilutions of test compounds and 50 µL of 0.02 M sodium phosphate buffer (pH 6.9 with 0.006 M sodium chloride) containing α-amylase solution (0.5 mg/ mL) were incubated at 25°C for 10 min. After pre-incubation, 50 µL of 1% starch solution in 0.02 M sodium phosphate buffer (pH 6.9 with 0.006 M sodium chloride) was added to each tube. The reaction was incubated at 25°C for 10 min. The reaction was terminated by adding 100 µL of dinitro salicylic acid (DNS) colour reagent. Microplates were then incubated (85-90°C) for 10 min to develop colour and left to cool room temperature and diluted with 105 µL of distilled water. Enzymatic activity was quantified by measuring the absorbance at 540 nm in a microtiter plate reader (Bio-TEK, USA). Acarbose was used as standard and experiments were done in triplicates. The inhibition percentage was calculated as a formula:

$$\% \text{ inhibition activity} = [A_C - A_S]/A_C \times 100$$

2.4.4 β-Glucosidase inhibition activity

The β-glucosidase inhibition study was carried out according to the reported methods [36] and was used with some modification for the β-glucosidase inhibition activity. In brief, β-glucosidase of sweet almonds lyophilized powder for extra pure powder was dissolved in 100 mL assay buffer (pH 7.0) and sonicated properly at 4 °C. After sonication, the suspension was centrifuged (4,000 rpm, 4 °C, 30 minutes) and the resulting supernatant was used for the assay. Transfer 20 µL distilled water (H_2O) to two wells of a clear bottom 96-well plate. A reaction mixture containing 50 µL of buffer (50 mM; pH 6.8), 50 µL of P-Nitrophenyl-β-D-Glucopyranoside extra pure and 50 µL sample of varying concentrations (100-800 µg/mL) was pre-incubated for 20 min at 37 °C and then 50 µL of 3 mM pNPG was added to the mixture as a substrate. After incubation at 37 °C for 30 min, β-glucosidase enzymatic activity was determined by measuring the absorbance at 405 nm in a microtiter plate reader (Bio-TEK, USA). Acarbose was used as the control. The inhibition percentage against β-glucosidase by the compounds was evaluated using the equation:

$$\% \text{ inhibition} = [A_C - A_S]/ A_C \times 100$$

2.5 Computational Studies

All DFT calculations were performed using the GAUSSIAN 09 program package [37] by the DFT/B3LYP method [38-40]. The input files of the vanadium(V) complexes were prepared with Gauss View 5.0.9 [41]. During optimization, the anion was ignored and only the cationic complexes were taken into account. The electronic excitations of the vanadium(V) complexes were made by using the time-dependent density functional theory (TD-DFT)/B3LYP method with a LANL2DZ basis set in the gas phase [42]. Using the time-varying density functional theory, the vertical electronic excitation based on the optimized geometry of B3LYP is calculated [43] in DMSO with a conductor-like polarizable continuum model (PCM) [44].

3 Results and discussion

The Schiff base was obtained by mono condensing of equimolar ethanolic solution of nicotinic acid hydrazide and o-vanillin (Scheme 1). Six new complexes of dioxide ((Z)-N'-(2-hydroxy-3-methoxybenzylidene) nicotine hydrazide) vanadate(V) salts with Imidazole (ImH), 2-methylimidazole (2-MeImH),1-methylimidazole (M-ImH), 2-ethylimidazole (2-EthImH), benzimidazole (BenzImH) and 2-methylbezimidazole (2-MeBenzImH) counter ions were synthesized using Scheme 2 and 3 in good yield. Yellow coloured polycrystalline complexes were obtained. These were characterized using elemental analysis, FTIR, single X-ray analysis and NMR techniques. All the complexes are air-stable. The complexes are insoluble in water, hexane, benzene and petroleum ether but soluble in DMSO, DMF, and acetonitrile. The room temperature magnetic susceptibilities values indicate the diamagnetic character of these complexes. Thus, all complexes are in a +5-oxidation state. Several efforts for recrystallization for complexes **3**-**6** were made but, single crystals suitable for X-ray analysis were not obtained.

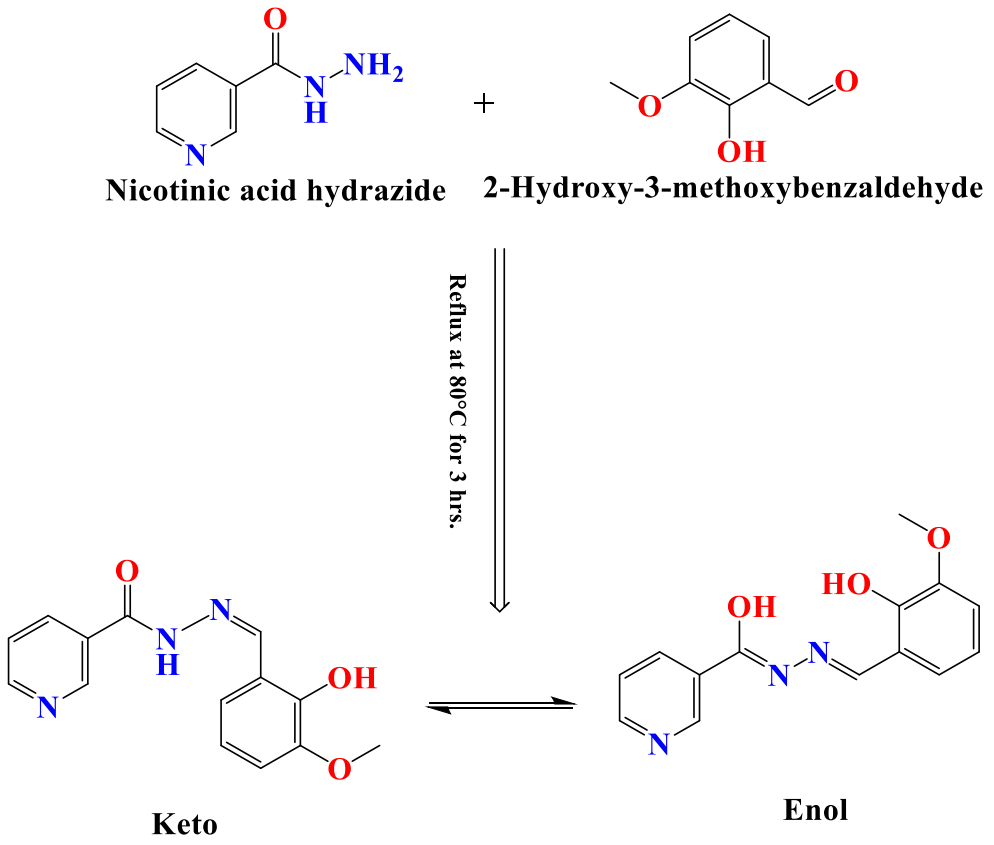

H_2L = (*Z*)-*N*'-(2-hydroxy-3-methoxybenzylidene)nicotinohydrazide

Scheme 1 Structure of Schiff base ligand **H_2L**.

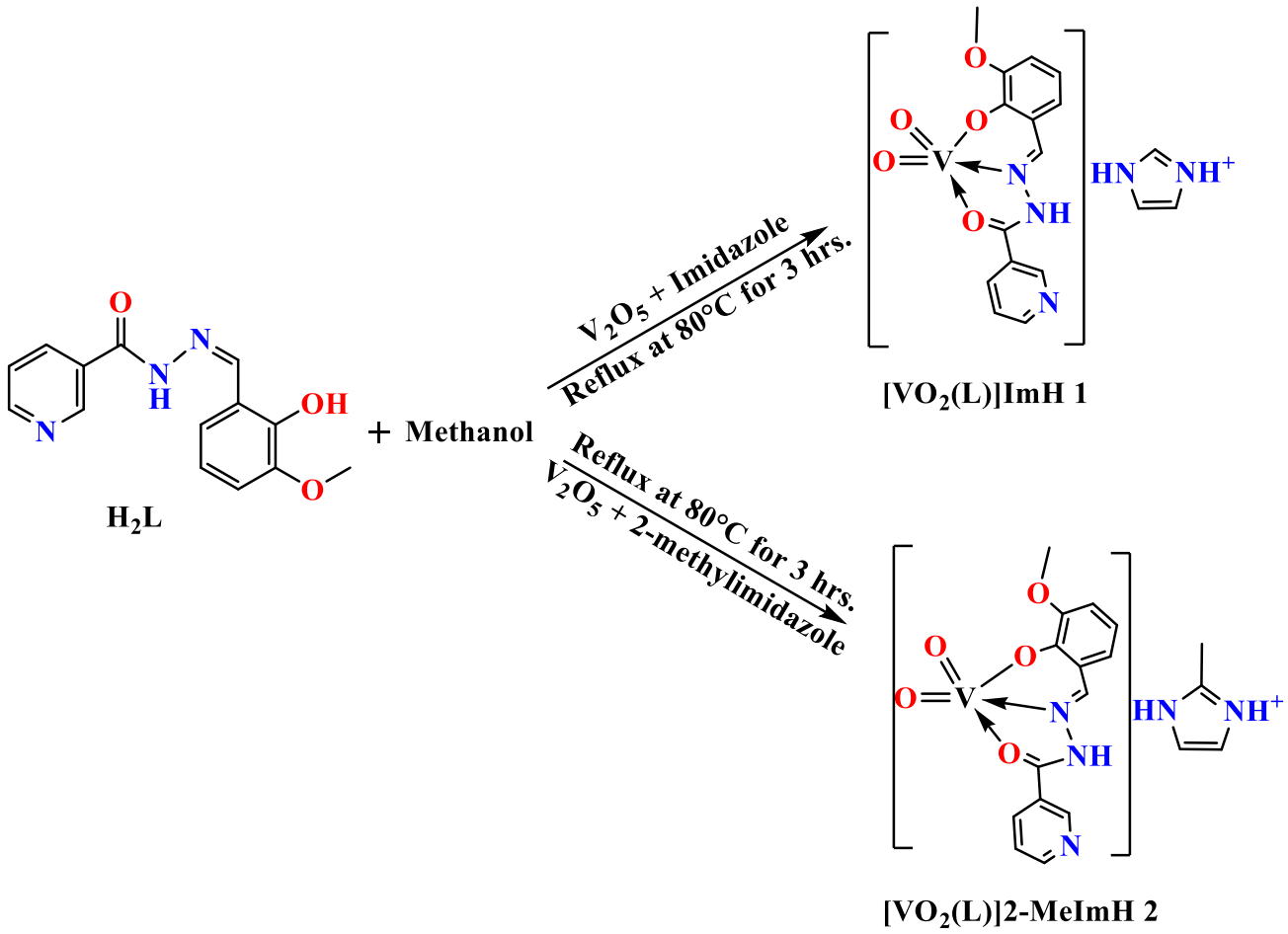

Scheme 2 Synthetic route of complexes **1** and **2**.

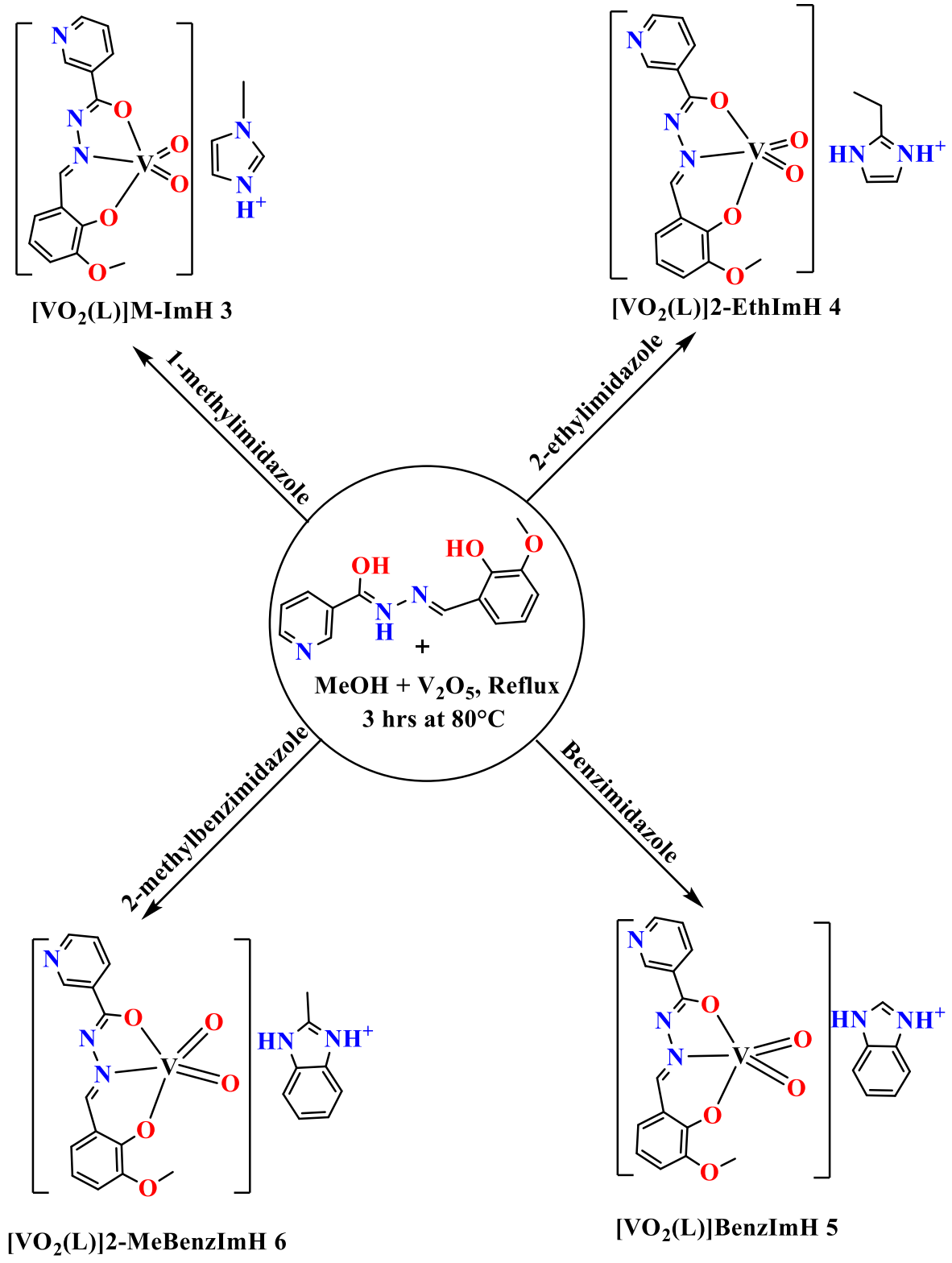

Scheme 3 Synthetic route of complexes **3-6**.

3.1 NMR spectral study

The ^{1}H NMR spectra of Schiff base (H_2L) have been recorded in DMSO-d_6. The phenolic (-OH) protons of the H_2L appeared at 12.2 ppm and hydrazide (-NH-) proton appear in 10.8 ppm. ^{1}H NMR spectrum is shown in Fig. 1. The spectrum shows a peak at 8.7 ppm which is assigned to azomethine (-CH=N-) proton. Thus, the ligand spectrum of the Schiff base suggests existing only enol form in solution. The spectrum show (-CH-OCH_3) peaks was obtained at 7.5 ppm All aromatic peaks are indicated in 9- 6.8 ppm. The protons of methoxy (-OCH_3) moiety of H_2L appeared at 3.8 ppm [45, 46]. ^{13}C NMR spectra of Schiff base (H_2L) has been recorded in DMSO-d_6. ^{13}C NMR Carbonyl (-C=O) and azomethine (-CH=N-) carbon peak is indicated in 161 and 152 ppm. The (-CH-OCH_3) peak was obtained at 124 ppm. Similarly, aromatic peaks are obtained in the range of 148-114 ppm. ^{13}C-NMR of ligand H_2L methyl (-OCH_3) carbon peak appeared in 56 ppm. ^{13}C NMR spectrum is shown in Fig. 2.

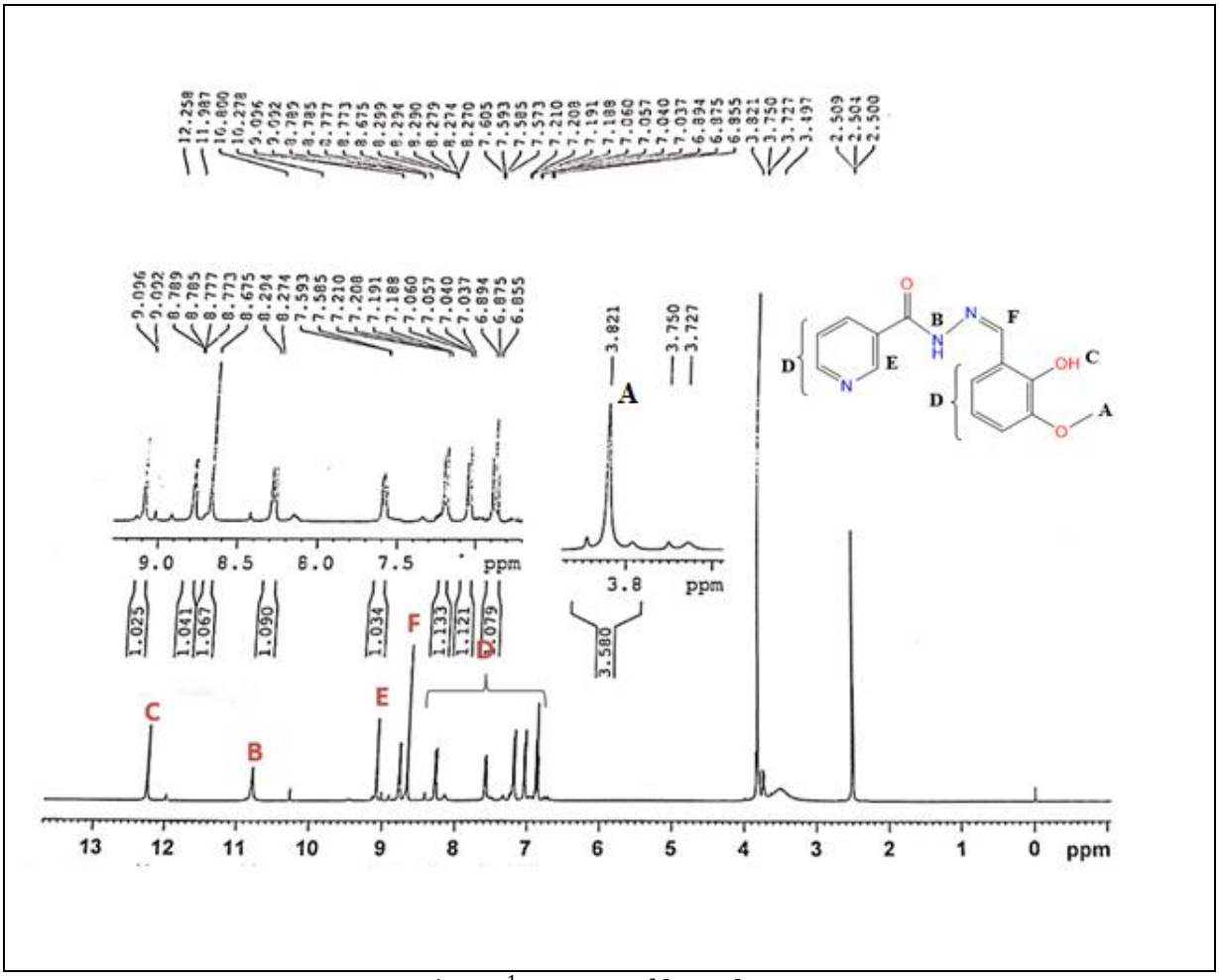

Fig. 1. ^{1}H NMR of ligand **H_2L**.

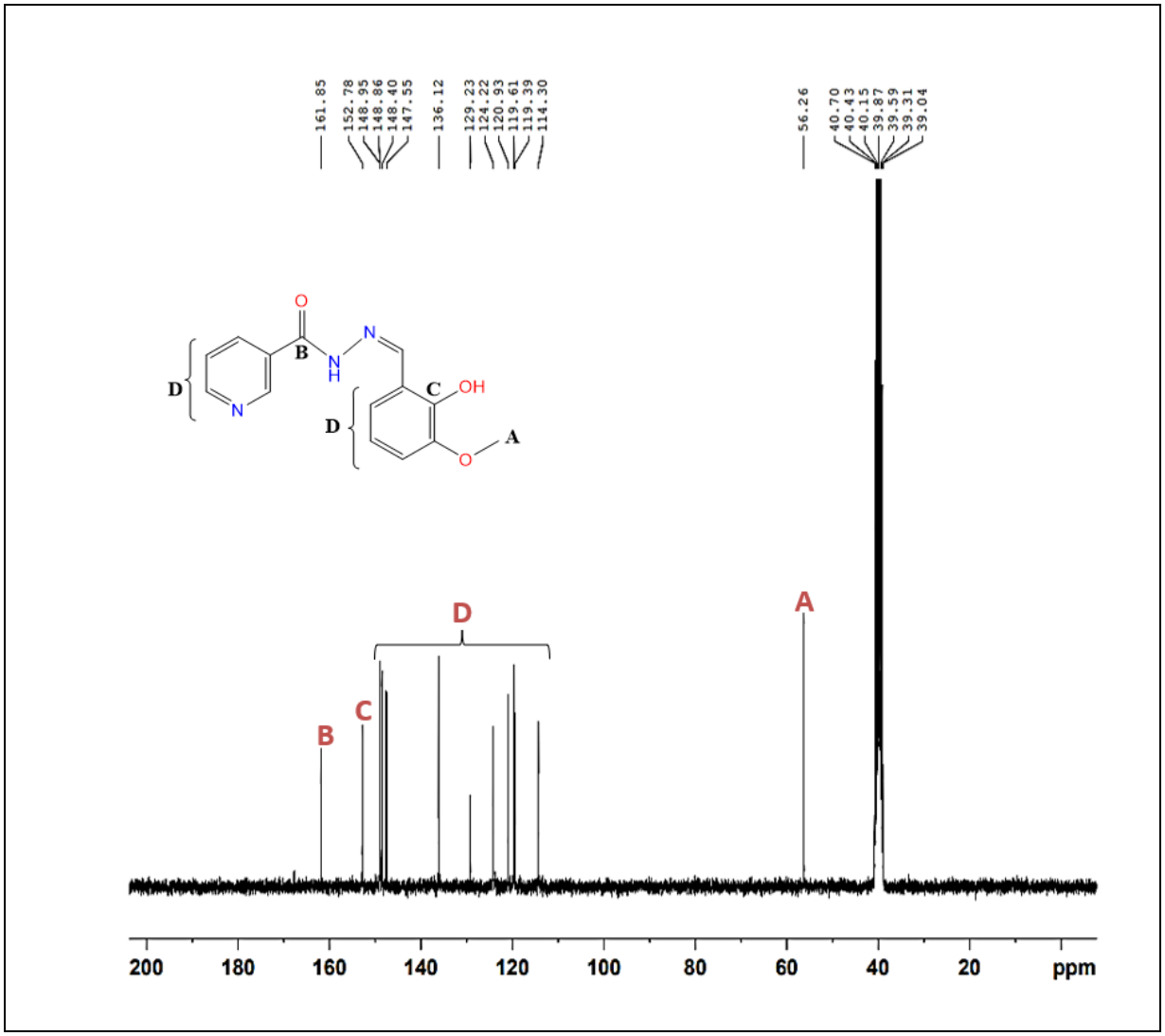

Fig. 2. ^{13}C NMR of ligand **H_2L**.

3.2 Magnetic susceptibility

The room temperature susceptibilities values reveal the diamagnetic nature of complexes **1-6**, conforming to the +5-oxidation state of the vanadium centre (d^0).

3.3 Molar conductance

The molar electrical phenomena values of complexes **1-6** were also measured in 1.0×10^{-3} M DMSO solution. The observed range of molar conductance is 70.86-84.21 Ω^{-1} cm^2 mol^{-1}. These values are lower than the molar conductance for a 1:1 electrolyte [47,48]. Probably these complexes show very low mobility because of the bigger size of their counter

ions in the solution. Therefore, these complexes due to their bigger size have slow motion in solution and furnish less molar conductance [48].

3.4 FTIR Spectral studies

The FTIR spectra of complexes were recorded in the 400-4000 cm^{-1} range in the KBr pellet. Some selected FTIR spectral data of ligand H_2L and complexes **1-6** are given in Table 1. A comparison of the FTIR spectral data with these of the complexes reveals that the H_2L ligand is coordinated to the vanadium ions in the enol form in complexes. The FTIR spectra of ligand and complexes are shown in Fig. 3-9.

Table 1 FTIR spectral data for complexes **1-6** (ν in cm^{-1}).

Compound	ν(N-H)	ν(>C=N)	ν(C-O)	ν(V=O)	ν(V-O)	ν(V-N)
H_2L	3368	1672	-	-	-	-
1		1656	1223	951	465	424
2		1635	1248	967	465	424
3		1623	1254	965	474	436
4		1632	1250	942	459	410
5		1633	1281	950	459	425
6		1633	1280	947	470	442

The FTIR spectrum of the H_2L ligand show stretching vibration at 3270 due to ν(N-H) stretching respectively [49]. The disappearance of this band in complexes suggests the replacement of proton (H) by the vanadium ion. The bands appearing in the range 1250-1280 cm^{-1} are assigned to the ν(C-O $_{enolic}$) mode [50]. The stretching vibration of the >C=N group, which shifts to lower wave number in complexes, suggestive of the coordination of the azo-methine nitrogen to the vanadium centre [51-54]. The strong new bands found in complexes in the region at 947-950 cm^{-1} are assigned to V=O group stretching vibrations, indicating the dioxidovanadium of the vanadyl group [55-60]. Two weak nonligand bands as shown in Table 1 appear in the low wave number region 453-473 cm^{-1} and 410-442 cm^{-1} due to ν(V-O) [61, 62] and ν(V-N) [63] stretching vibrations, respectively.

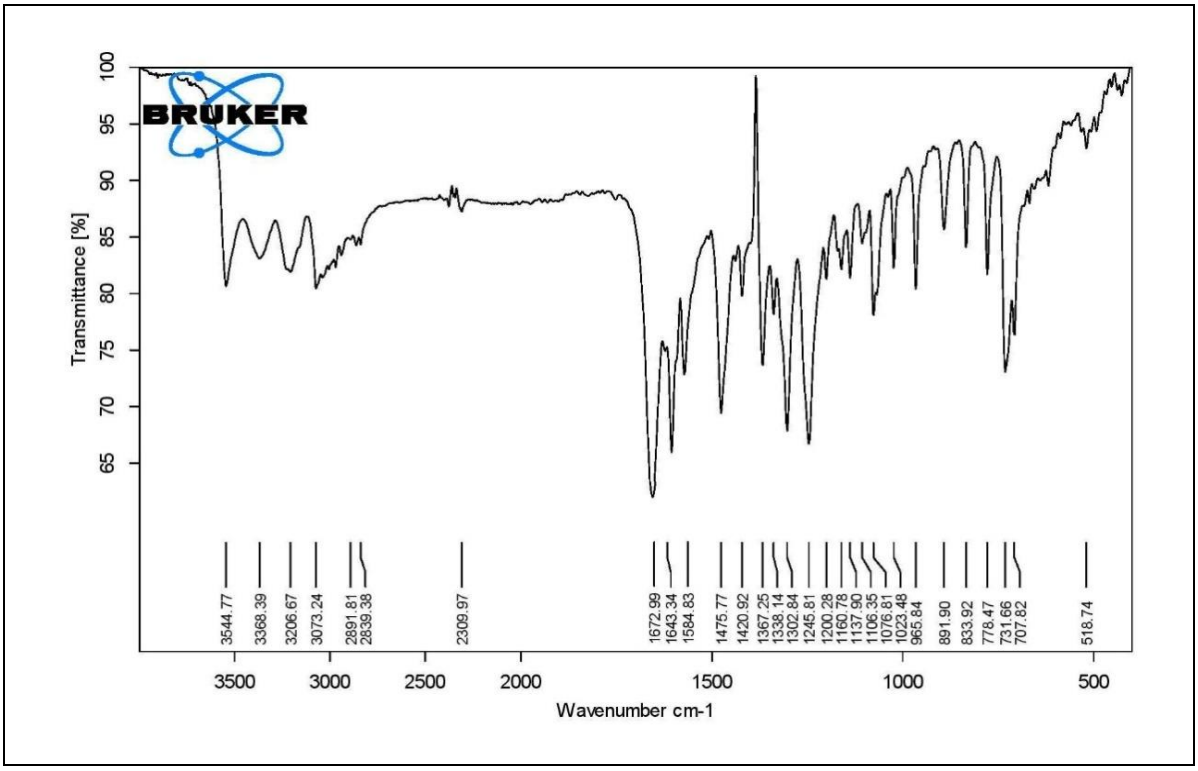

Fig. 3. FTIR spectrum of ligand **H_2L**.

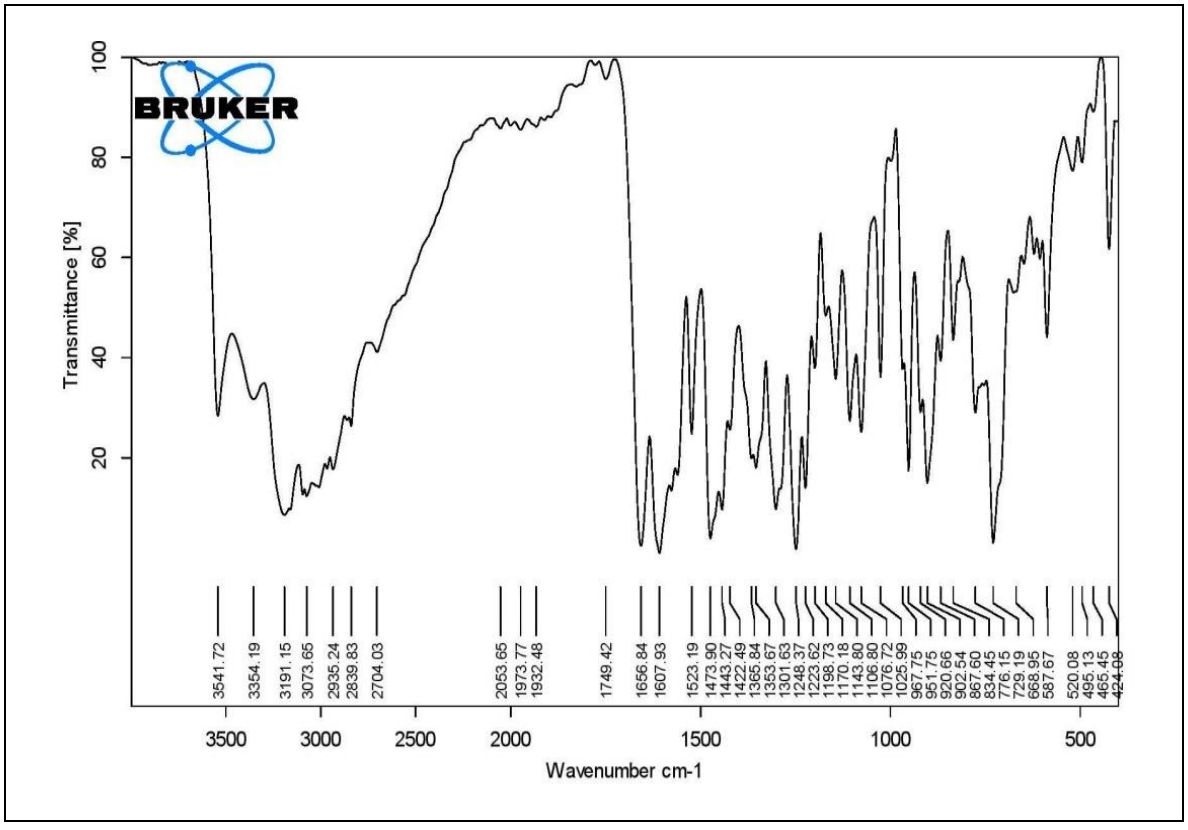

Fig. 4. FTIR spectrum of complex **1**.

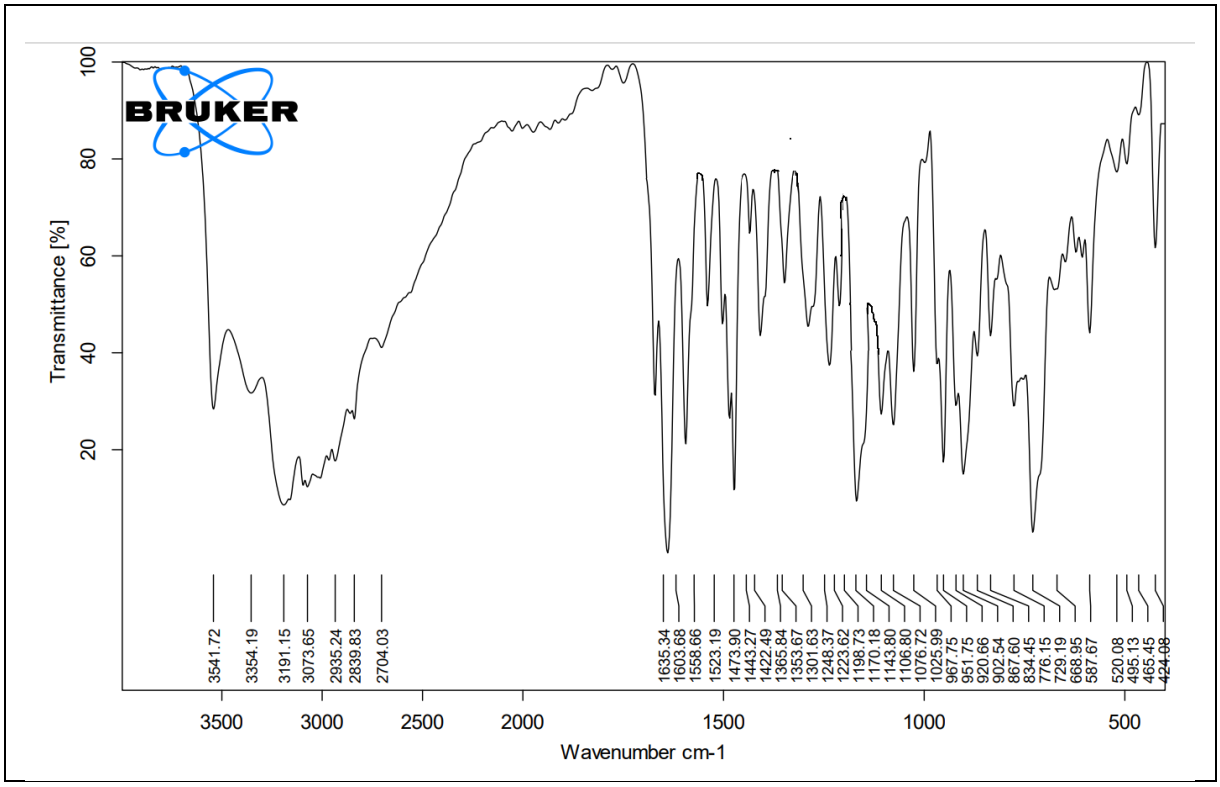

Fig. 5. FTIR spectrum of complex **2**.

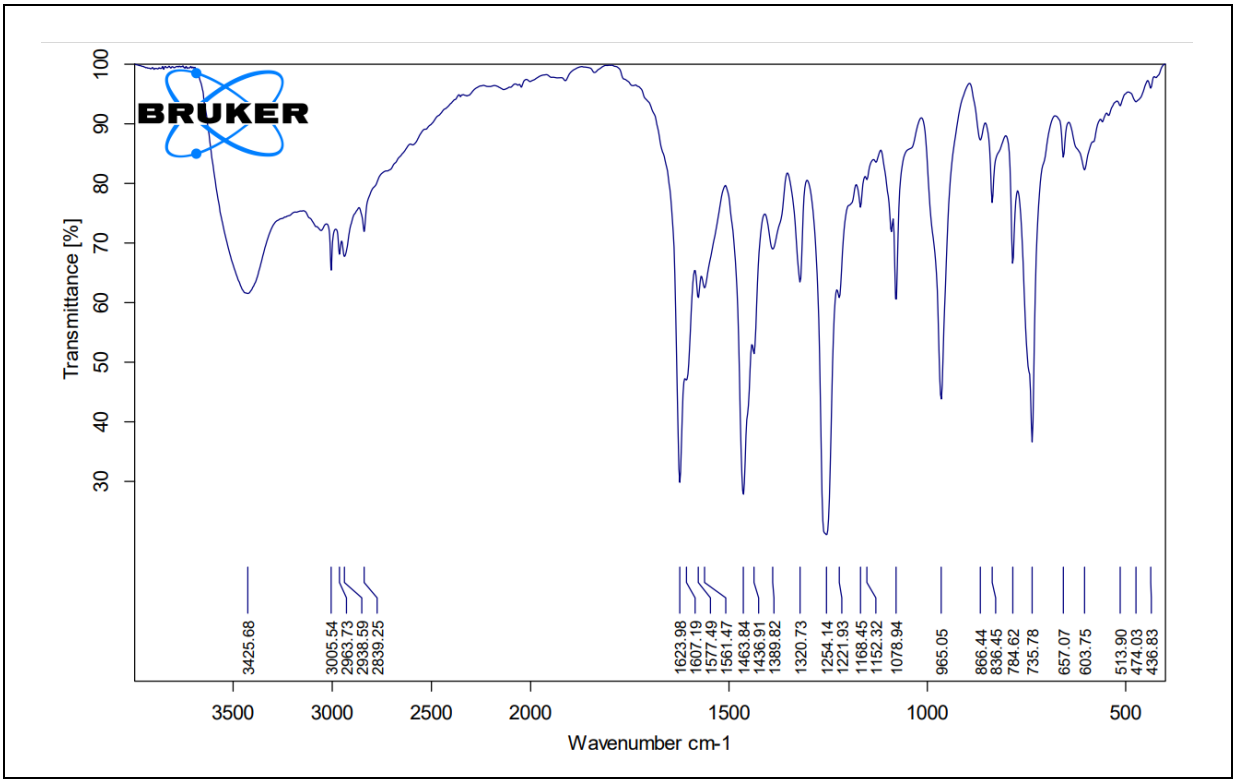

Fig. 6. FTIR spectrum of complex **3**.

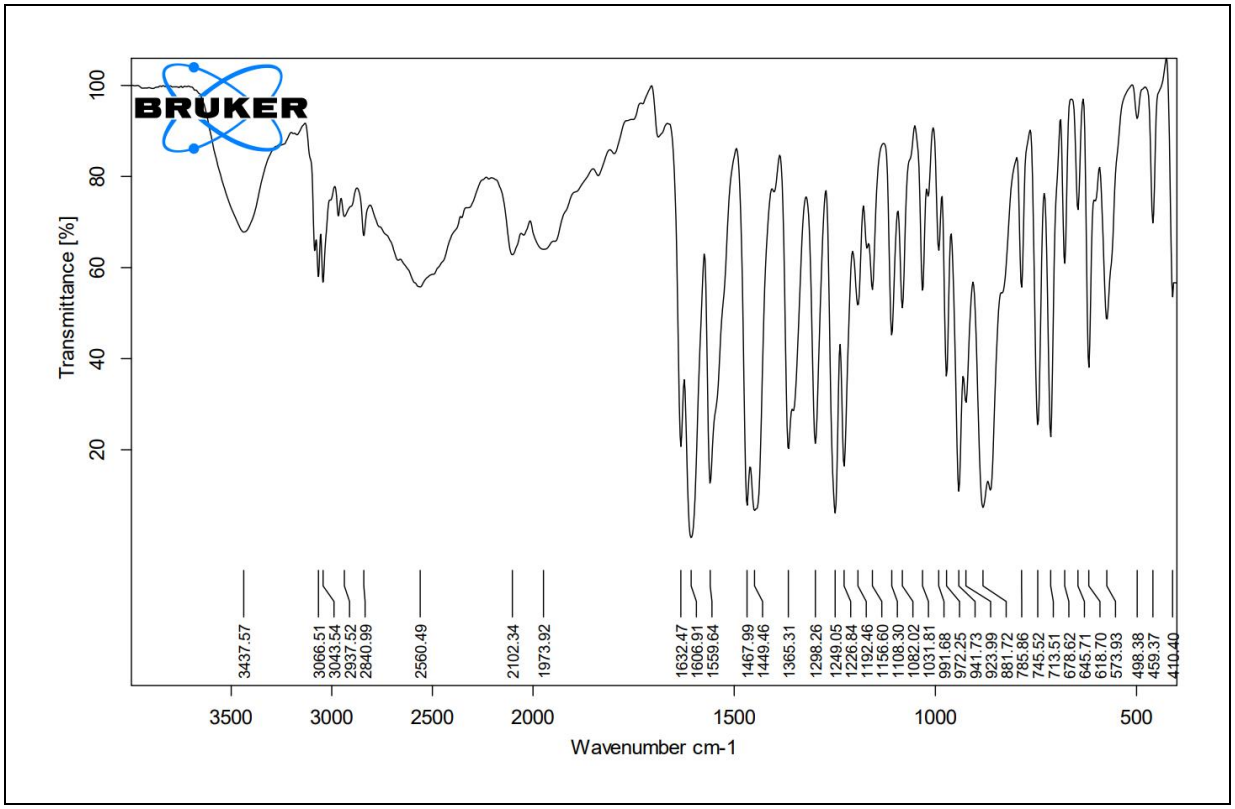

Fig. 7. FTIR spectrum of complex **4**.

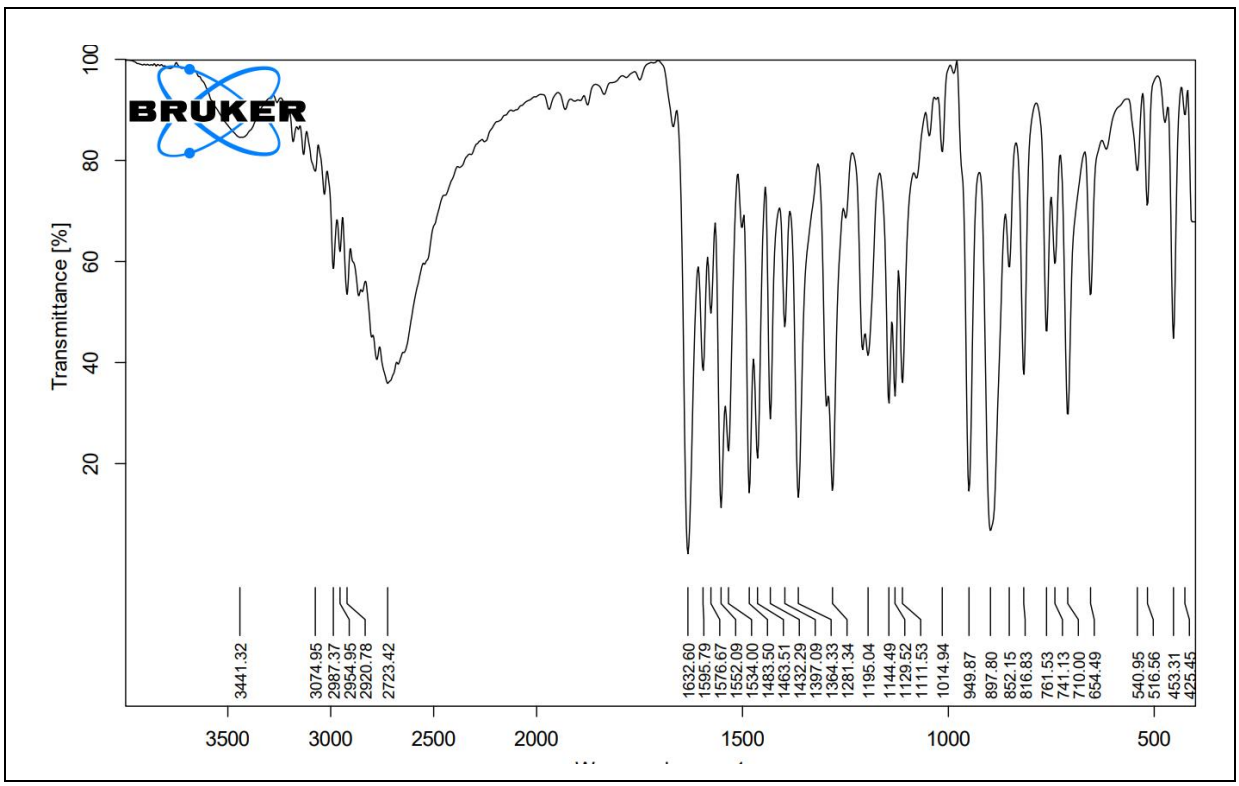

Fig. 8. FTIR spectrum of complex **5**.

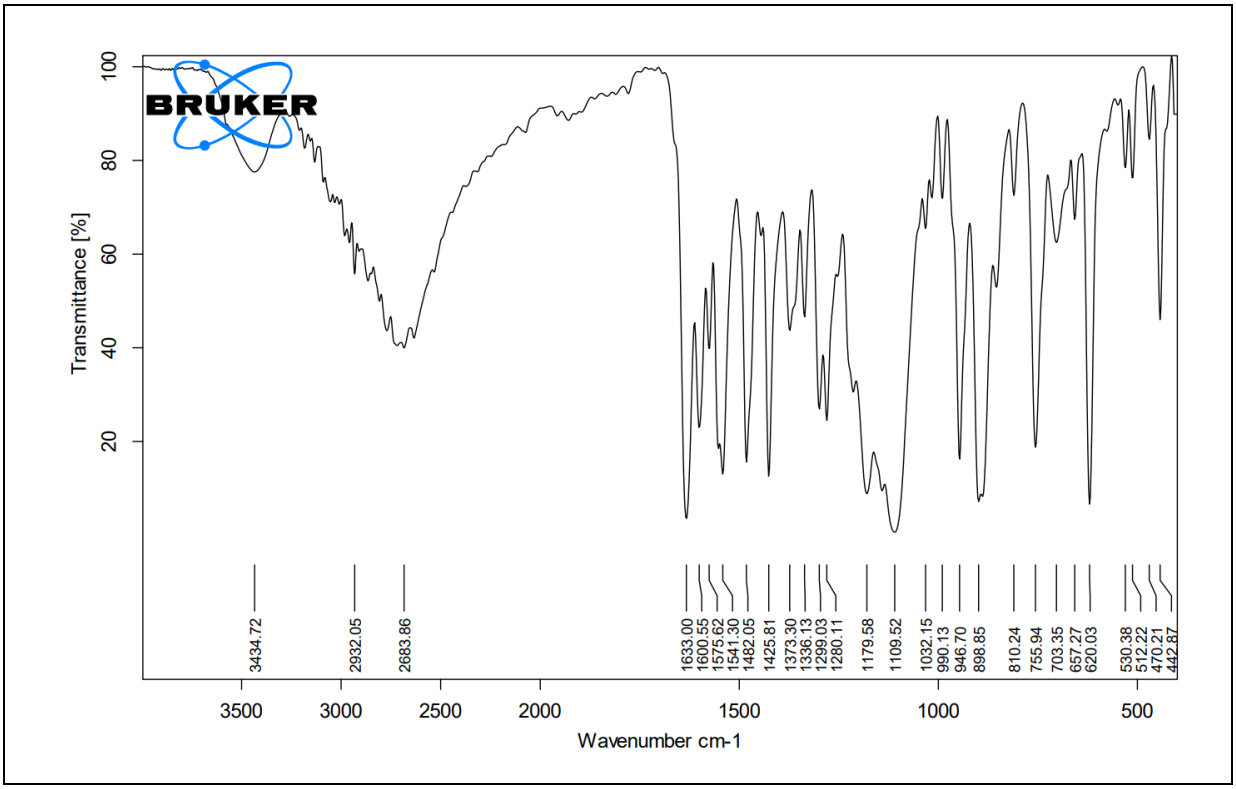

Fig. 9. FTIR spectrum of complex **6**.

3.5 Electronic spectral studies

Electronic spectra of both complexes were recorded using DMSO solutions [3×10^{-3} M] at RT. Spectral features of both complexes **1** and **2** are almost similar. The spectra of both complexes are shown in Fig. 10 the electronic spectra of complexes are possibly due to the ligand-to-metal charge transfer (LMCT) to empty d-orbitals of the metal [64-67]. As vanadium(V) complexes possess a d^0 configuration, d-d bands are not expected for the present complexes. Therefore, only the transition the other highest energy absorption observed at 338 in **1** and 348 in **2** nm. Most likely due to the ligand-centered transition (π-π^*) bands at ~413 nm are assigned to charge transfers (LMCT) [68, 69].

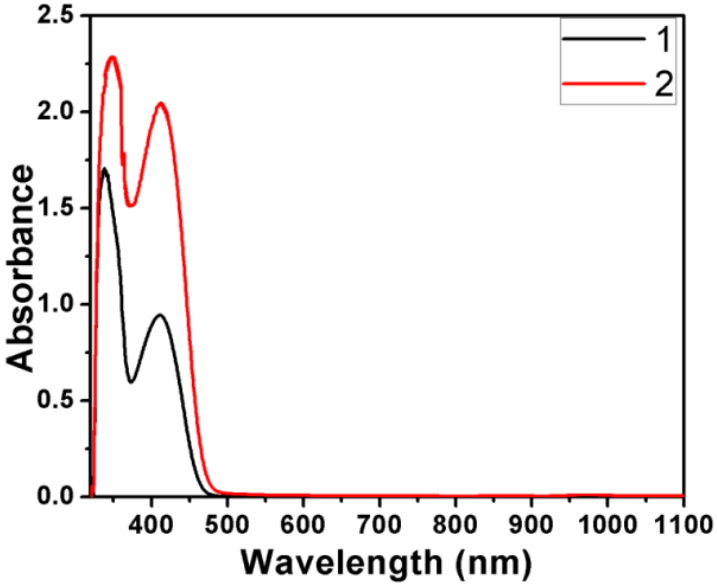

Fig. 10. Electronic spectra of complexes **1** and **2**.

Electronic spectra of complexes **3-4** were measured in DMSO solution (1.0×10^{-3} M) and spectra of complexes are shown in Fig. 11. The electronic spectral data of the complexes are collected in Table 2. The complexes reveal bands in the range 335-339 nm. The high energy bands are assigned to an intra ligand charge transfer (ILCT) bands [70], while bands at 415 ± 2 nm are assigned to a ligand to metal charge transfer (LMCT) [71-78] it originates from the lone pair of the p orbital of the phenate oxygen atom to the empty d orbital of the vanadium (V) center. The d-d bands are not shown by these complexes being the V(V) d^0 system.

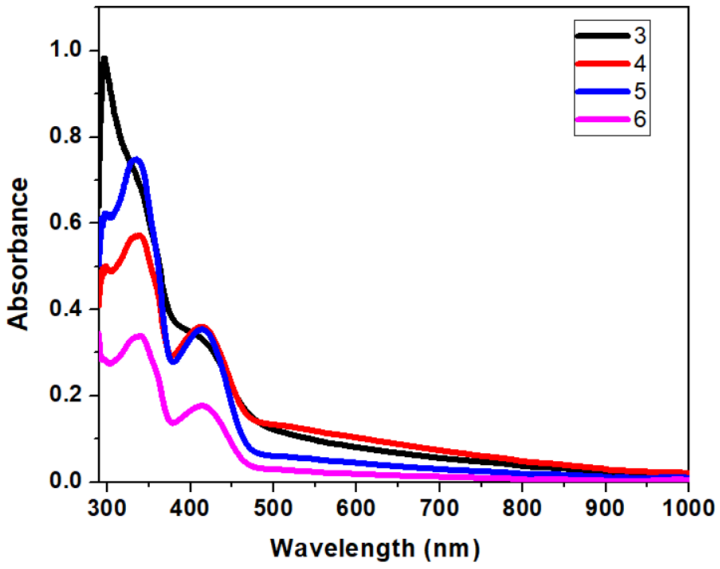

Fig. 11. Electronic spectra of complexes **3-6**.

Table 2 UV-Visible spectral data of complexes **1-6**.

Complex	λ_{max} (nm)	
	ILCT	**LMCT**
1	338	420
2	342	417
3	337	417
4	335	413
5	337	415
6	339	417

3.6 Electrochemistry studies

Electrochemical studies of these complexes were also explored using cyclic voltammetry (CV) and differential pulse voltammetry (DPV). Electrochemical data are presented in Table 3. The cyclic voltammetry of complexes **1** and **2** have been recorded in DMSO solution (1.0×10^{-3} M) using 0.1 M tetrabutylammonium perchlorate (TBAP) as a supporting electrolyte with Ag/AgCl as the reference electrode (Fig. 12(a)). CV experiments of **1** exhibited V^{V}/V^{IV} reductive responses with potential fairly on the negative side (-0.754 V). Its anodic counterpart is not visible. In complex **2** no such reduction wave was observed. We believe that the presence of an electron-donating methyl group in substituted imidazole in this complex increased the electron density at the vanadium centre and therefore better stabilize the V^{V} state [79-82]. DPV of these complexes is shown in Fig. 12(b). DPV exhibited similar observations. Complex **1** showed two reduction waves at -0.512 V due to V^{V}/V^{IV} reduction response and observation of highly negative potential is due to the reduction of anionic ligand [83-85]. Whereas complex **2** showed only one reduction at -0.625 V.

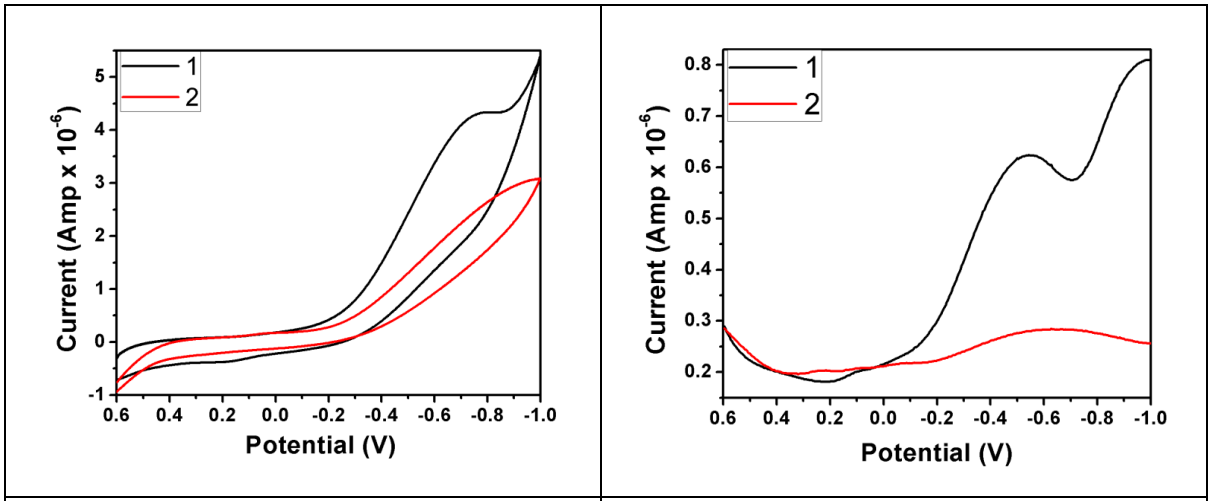

Fig. 12(a) Cyclic voltammogram (CV) and **(b)** Differential pulse voltammogram (DPV) of complexes **1** and **2**.

The cyclic voltammogram of complexes **3-6** shows one irreversible cathodic reduction peak. Measured CV and DPV are shown in Fig. 13. These are irreversible in redox waves. The cathodic peak in all the complexes **3-6** are assigned to the one-electron V(V)→V(IV) electrode process. These peak potentials (E_{pc}) are within the range of values for the reduction V(V)/V(IV) of hydrazone vanadium complexes [86]. Redox potentials (E_{pc} and E_{pa}) are an important parameter in such electron-transfer electrode reactions. DPV experiments showed similar observations. One reduction peak was observed for each complex (Fig. 13(a)) and DPV data are also given in Table 3. DPV is one of the most accurate electrochemical techniques and has received a great deal of attention in the present days.

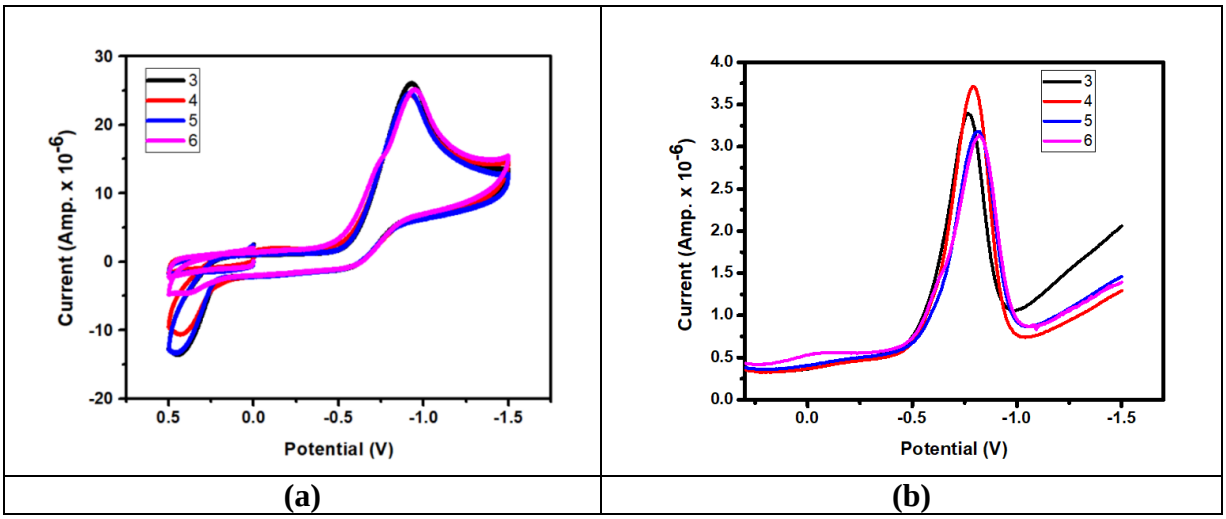

Fig. 13. Cyclic voltammogram (CV) and differential pulse voltammogram (DPV) of complexes **3-6**.

Table 3 Electrochemical data (in V) of complexes **3-6**.

Complex	E_{pc}	E_{pa}	ΔE_p	$E_{pc}^{1/2}$	D_{pc}	ΔD_{pc}
3	-0.924	-0.309	0.615	-0.616	-0.773	0.214
4	-0.980	-0.400	0.580	-0.690	-0.793	0.201
5	-1.010	-0.318	0.692	-0.664	-0.829	0.222
6	-1.014	-0.292	0.722	-0.653	-0.816	0.202

ΔD_{pc}= half peak width

3.7 Mass spectral analysis

The ESI-Mass of complexes **1-6** were carried out to get information about the molecular weight of the complexes. The mass of these complexes was matched with calculated values. The mass of complexes gives the molecular ions peaks in the form of $[M]^+$ and $[M + 1]^+$ ion in the positive mode ESI-Mass. The mass spectra of complexes are given in Fig. 14-19.

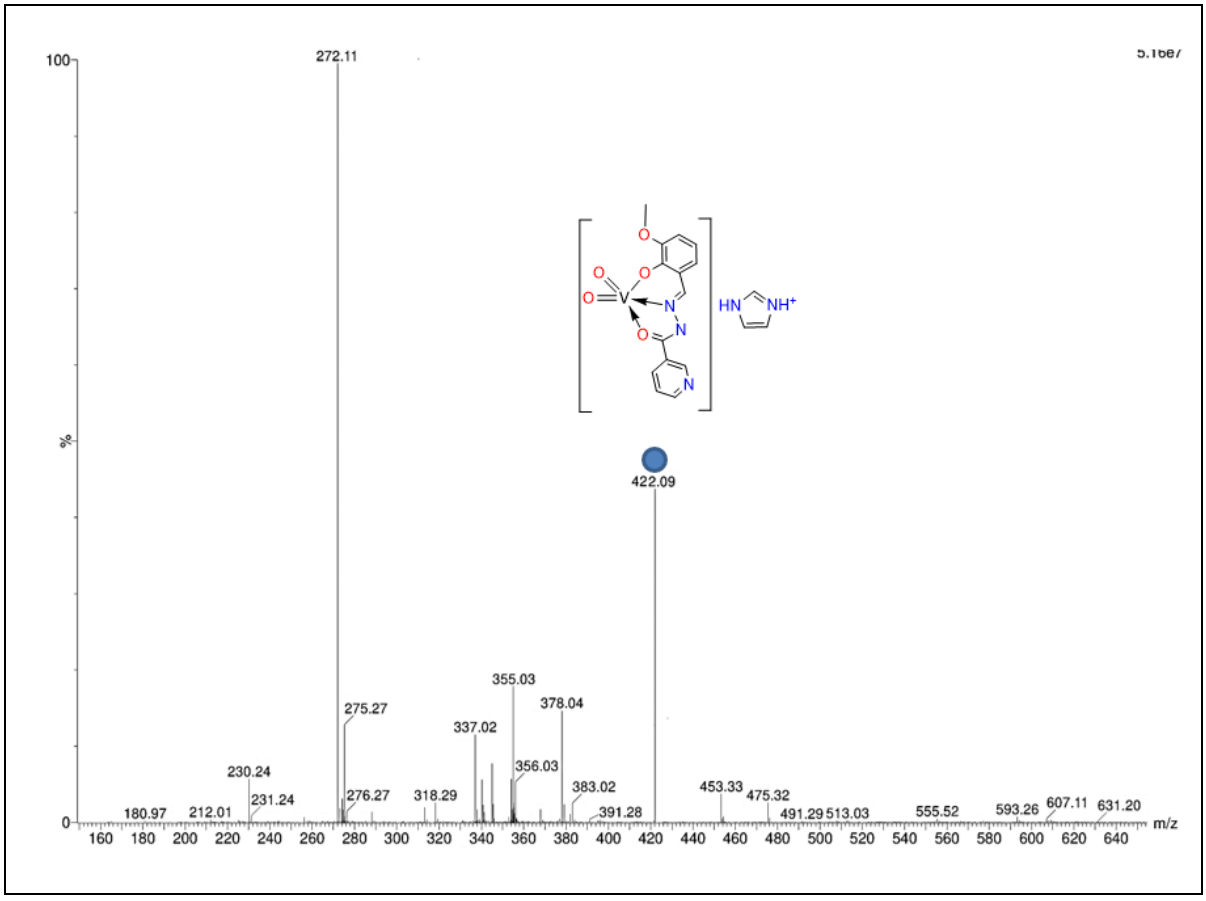

Fig. 14. Mass spectrum of complex **1**.

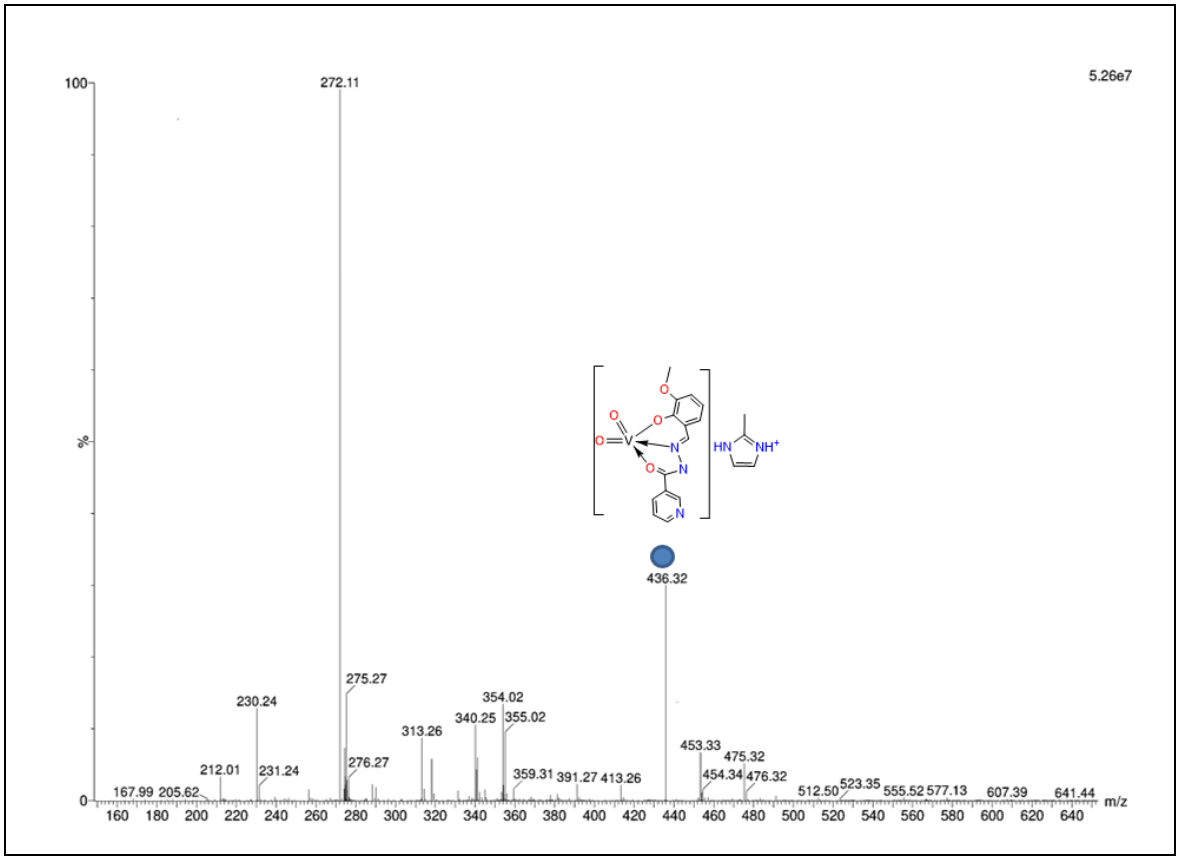

Fig. 15. Mass spectrum of complex **2**.

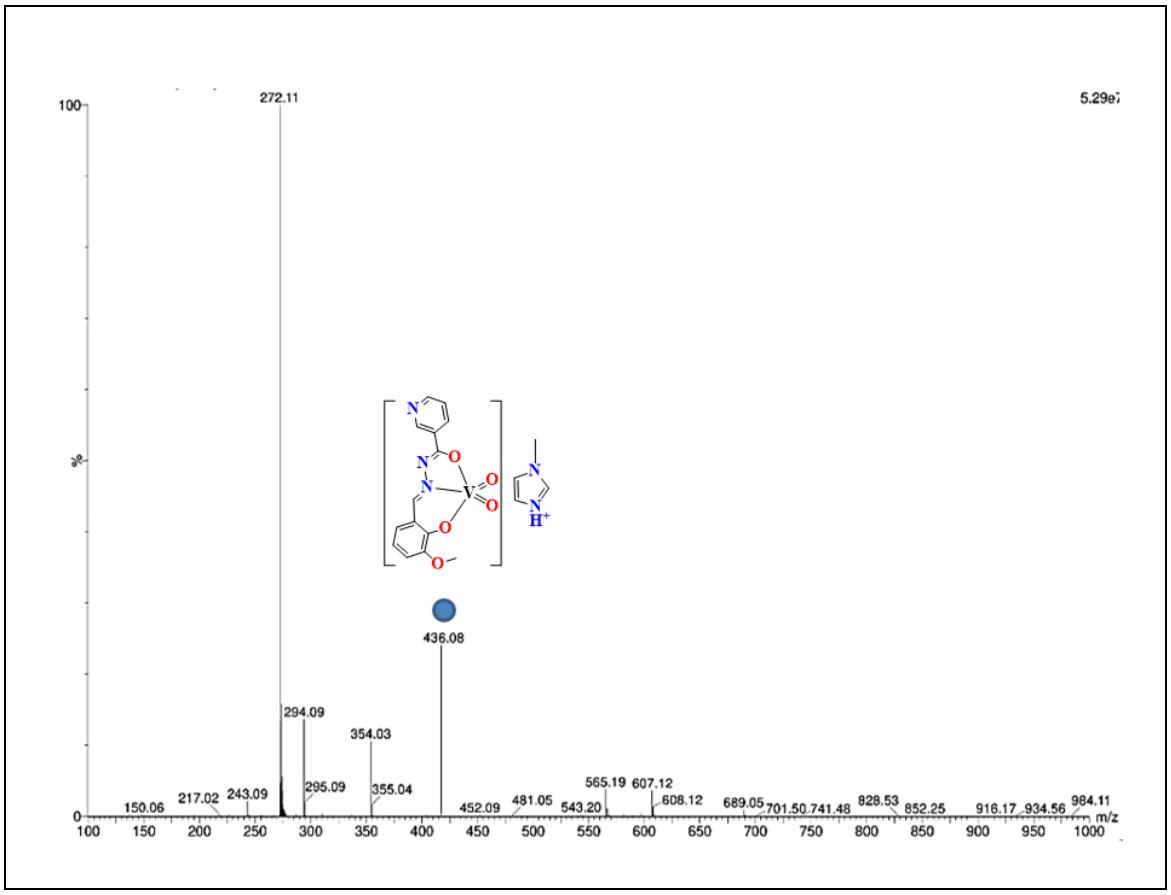

Fig. 16. Mass spectrum of complex **3**.

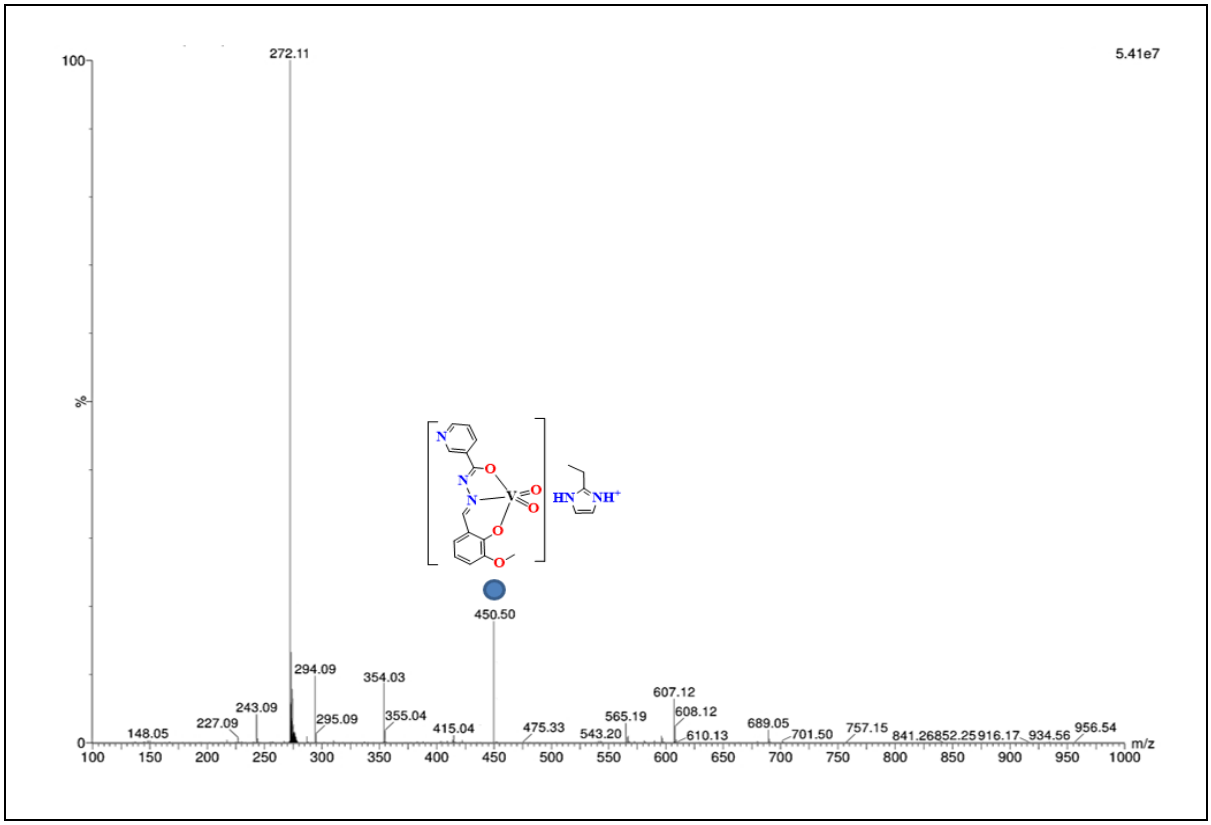

Fig. 17. Mass spectrum of complex **4**.

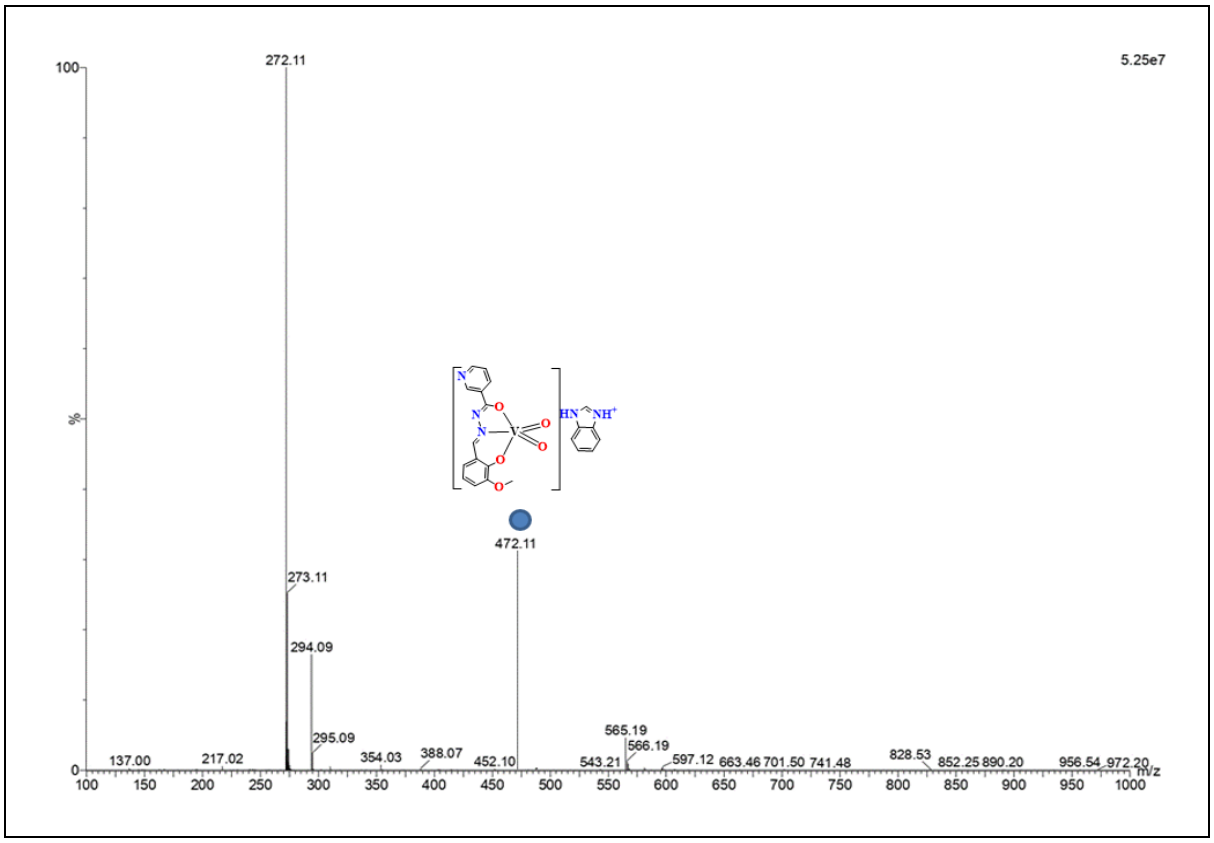

Fig. 18. Mass spectrum of complex **5**.

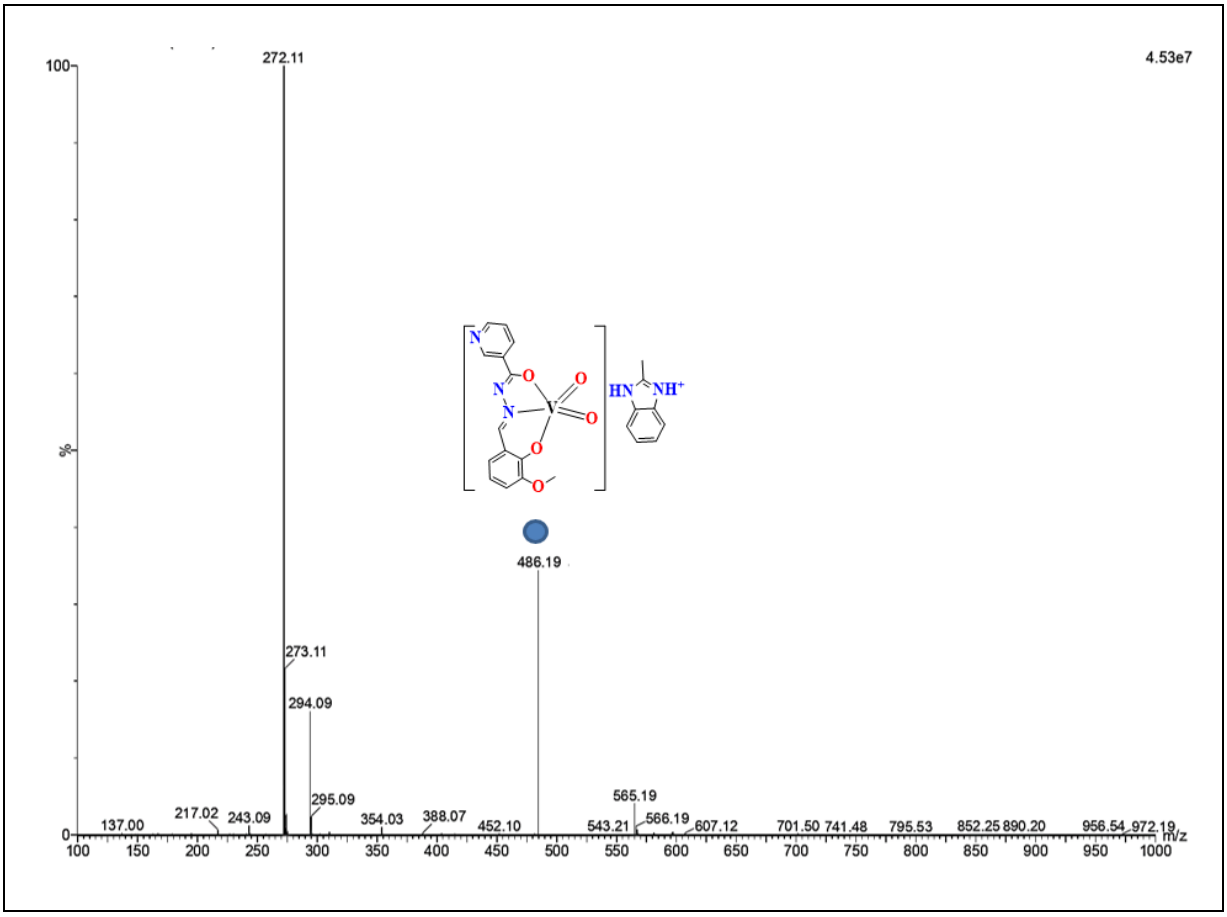

Fig. 19. Mass spectrum of complex **6**.

3.8 X-ray structures of complexes 1 and 2

The geometry of both complexes has been determined by single-crystal X-ray analysis. The molecular structure and the atom-labelling scheme of both complexes are shown in Fig. 20-27. Table 4 gives information about the crystal. Table 5 summarizes the bond distances and bond angles. In Table 6 hydrogen bonding is given.

Complex **1** crystallizes in the *P-1* triclinic space group. The molecular structure of this complex contains two asymmetric units. In the structure of **1,** the vanadium metal is pentacoordinated by two oxido groups and monoanionic tridentate ONO Schiff base ligand. The monoanionic tridentate L^- ligand spaus the meridonial sites. The coordination sphere of vanadium is distorted pyramidal, as ascertained by the structural parameter $\tau_5 = 0.124$ (0 for an ideal square pyramidal and 1 for an ideal trigonal bipyramidal) [87]. One imidazole molecule as lattice remains out the V^V coordination sphere. The oxido V=O bond distances remain in the range 1.597 (4)-1.648 (20) Å. These distances are comparable to those found in other V^VO- complexes with a square pyramidal VO_4N environment [70, 88-91]. Also, the V-

N (imine) bond distances (V1-N3 and V2-N6) are in the range found for other pentacoordinated Schiff base complexes [89-92]. In the lattice of the complex, strong bifurcated intermolecular H-bonding interactions (N···O distances: 2.226-2.246 Å) between the Schiff base oxygen atoms (O5, O6, O9 and O10) and the -NH- groups of imidazole. Thus, each –NH- group of imidazole forms a robust hydrogen bond of type $R_2^1(5)$ heterosynthon (Fig. 21). In the crystal lattice of **1**, extensive C-H···π (aryl) and O···π (metal chelate and aryl) are also observed (Fig. 22). A view of all cells of the complex **1** b-axis of shown in Fig. 23. The topology of the packing pattern of this complex is composed of four molecules.

Complex **2** crystallizes in the *P-1* space group. Complex **1** and **2** are iso-structural neutral molecules. The related structural parameters are given in Table 4. Crystal structure of **2** consists of a vanadium atom pentacoordinated by monoanionic tridentate Schiff base (L^-) and two dioxide group. In the crystal structure of this complex 2-MeImH remains as lattice molecule. Again, in this complex coordination geometry is a distorted square pyramidal, as ascertained by the structural parameter $\tau_5 = 0.04$. Other crystallographic parameters are very much similar to complex **1**. In this complex, each 2-MeImH moiety forms H-bonds of various types. N-H hydrogen atoms of 2-MeImH yield bifurcated robust intermolecular H-bonding with O of oxido L^- and forming heterosynthon of the type I $R_2^1(4)$ and type II $R_2^1(5)$. Therefore, the presence of two heterosynthons offer the homodimer formation of two co-crystals. Combined C-H and NH hydrogen atoms of m-ImH also form intermolecular H-bondings with O atom of oxido group of type III $R_2^1(6)$ (Heterosynthon) (Fig. 25). The molecular structure of **2** is also stabilized by various C-H···π (aryl metal chelates) and O···π (metal chelates) interactions by forming a supramolecular open framework (Fig. 26). A view of all cell of the complex **2** b-axis of shown in Fig. 27. Self-assembly *via.*, intermolecular non-covalent interactions is one of the powerful tools for designing and synthesizing polar crystals as well as enantioselective chiral host frameworks [93]. The topology of the packing of this complex contains two neutral molecules.

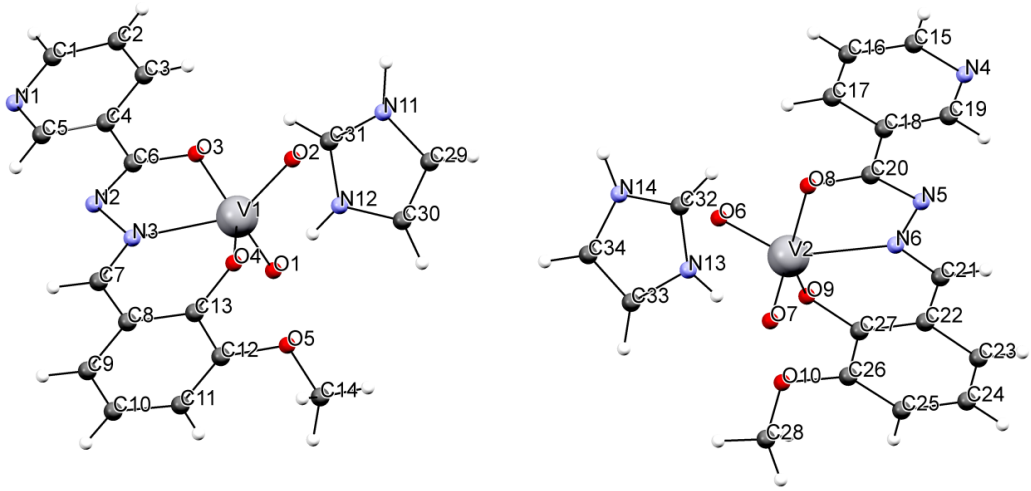

Fig. 20. Molecular structure of complex **1**.

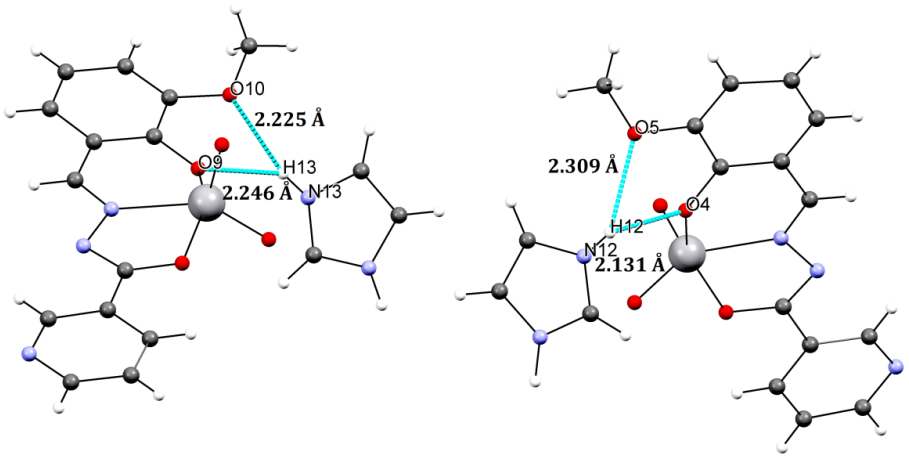

Fig. 21. The co-former ImH interaction with [VO_2(L)] showing $R_2^1(5)$ hydrogen-bonded motif in VO_2L.ImH stoichiometry co-crystals of complex **1**.

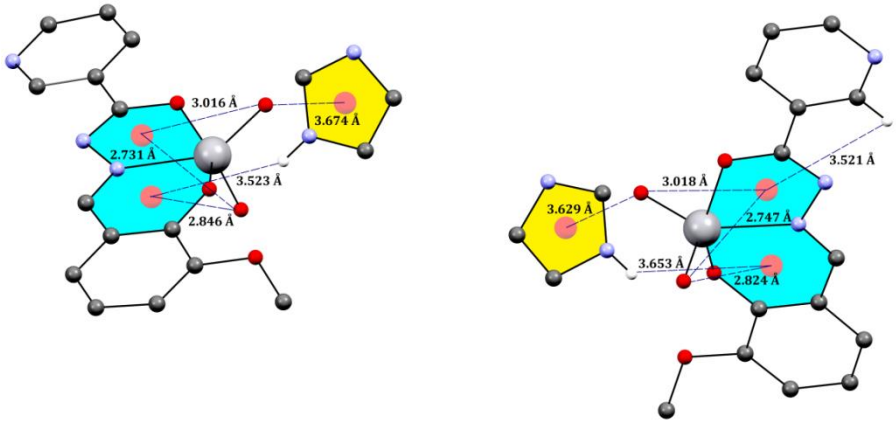

Fig. 22. N-H···π (metal chelate) and M-O···π (metal chelate and aryl) interactions of the complex **1**.

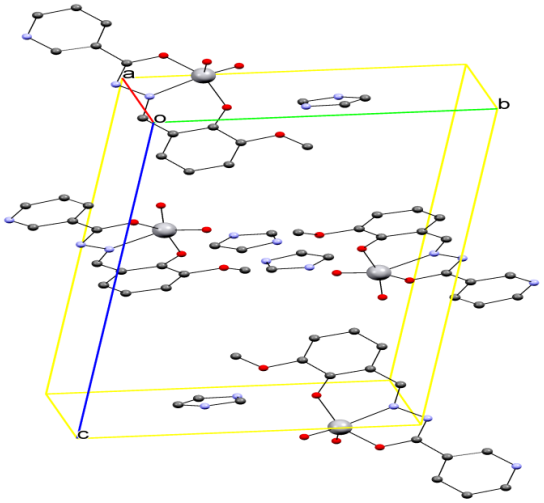

Fig. 23. Stereoscopic view of the cell of complex **1** down the b-axis (the a-axis is vertical).

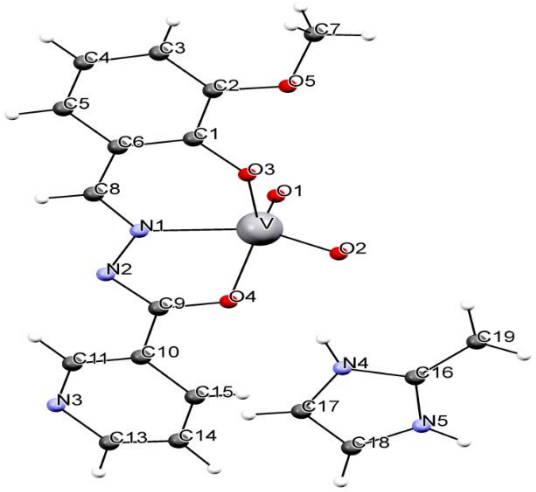

Fig. 24. Molecular structure of complex **2**.

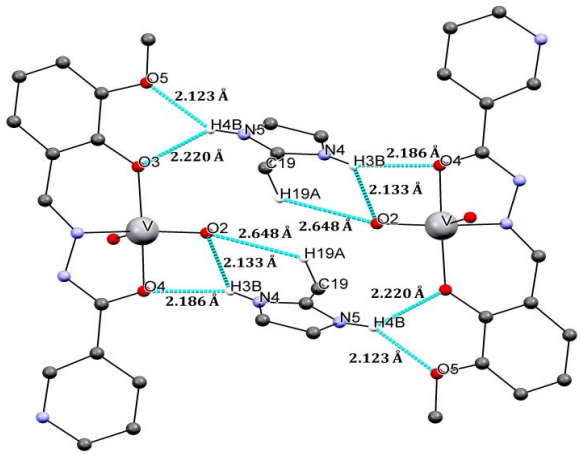

Fig. 25. The co-former m-ImH interaction with the two [VO_2(L)] showing $R_2^1(4)$ and $R_2^1(5)$ hydrogen-bonded motif in stoichiometry co-crystals of complex **2**.

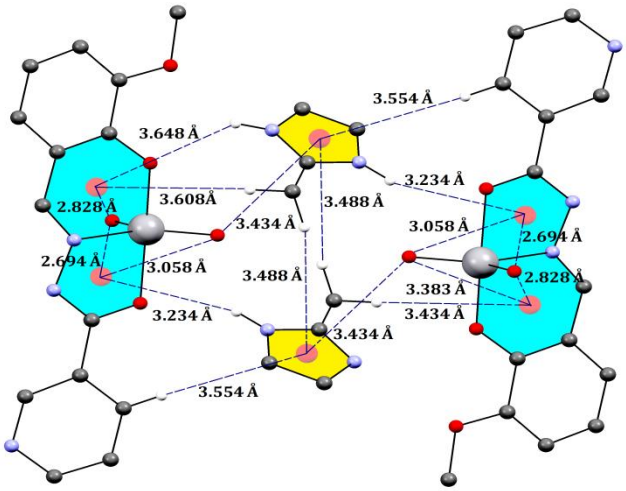

Fig. 26. Intermolecular C-H···π (metal chelate) interactions of complex **2**.

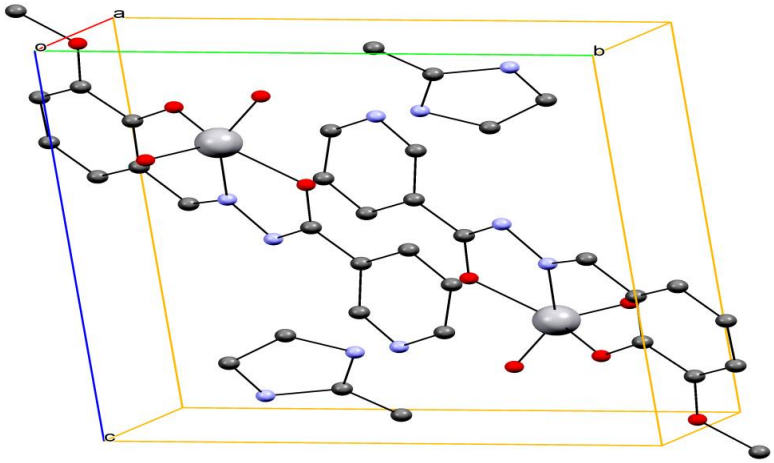

Fig. 27. Stereoscopic view of the cell of complex **2** down the b-axis (the a-axis is vertical).

Table 4 Crystal data and structure refinement for complexes **1** and **2**.

	Complex 1	**Complex 2**
Empirical formula	$C_{17}H_{16}N_5O_5V$	C18 H18 N5 O5 V
Formula weight	421.29	435.31
Temperature (K)	293(2)	100(2) K
Crystal system	Triclinic	Triclinic
Space group	P-1	P -1
a (Å)	9.3729(5)	8.4060(2)
b (Å)	11.6011(6)	9.6675(2)
c (Å)	17.2856(10)	11.5724(3)
α (°)	102.284(5)	86.0690(10)
β (°)	105.105(5)	75.2140(10)
γ (°)	90.342(5)	88.3340(10)

Volume (Å^3)	1769.32(17)	907.09(4)
Z	4	2
ρ_{calc}g/cm^3	1.582	1.594
μ/mm^{-1}	0.603	0.591
F(000)	864.0	448
Crystal size (mm^3)	0.15 × 0.15 × 0.10	0.22 x 0.15 x 0.06
Radiation	MoKα (λ = 0.71073)	
2Θ range for data collection (°)	6.28 to 51.98	2.506 to 33.239
Index ranges	-11 ≤ h ≤ 11, -14 ≤ k ≤ 14, -21 ≤ l ≤ 21	-12<=h<=12, -14<=k<=14, -17<=l<=17
Reflections collected	35005	45679
Independent reflections	6945 [R_{int} = 0.0603]	6947 [R(int) = 0.0775]
Data/restraints/parameters	6945/0/524	6947 / 0 / 264
Goodness-of-fit on F^2	1.117	1.077
Final R indexes [I>=2σ (I)]	R_1 = 0.0588, wR_2 = 0.1404	R1 = 0.0436, wR2 = 0.0897
Final R indexes [all data]	R_1 = 0.0709, wR_2 = 0.1535	R1 = 0.0591, wR2 = 0.0967
Largest diff. peak/hole (e Å^{-3})	0.84/-0.65	0.552 and -0.516

Table 5 Bond Length and bond angle for complexes **1** and **2**.

1					
Bond length					
	XRD	**DFT**		**XRD**	**DFT**
O(1)-V(1)	1.597(4)	1.590	N(6)-V(2)	2.132(4)	2.131
O(2)-V(1)	1.648(3)	1.645	O(6)-V(2)	1.639(3)	1.634
O(3)-V(1)	1.965(3)	1.965	O(7)-V(2)	1.605(4)	1.600
O(4)-V(1)	1.928(3)	1.926	O(8)-V(2)	1.966(3)	1.969
N(3)-V(1)	2.129(4)	2.120	O(9)-V(2)	1.917(3)	1.919
Bond angle					
O(1)-V(1)-O(2)	109.5(2)	109.5	O(7)-V(2)-O(6)	109.4(2)	109.41
O(1)-V(1)-O(4)	102.41(18)	102.2	O(7)-V(2)-O(9)	101.85(17)	101.81
O(2)-V(1)-O(4)	96.01(16)	96.09	O(6)-V(2)-O(9)	95.70(16)	95.72
O(1)-V(1)-O3)	102.83(17)	102.86	O(7)-V(2)-O(8)	103.61(17)	103.61
O(2)-V(1)-O3)	91.40(16)	91.46	O(6)-V(2)-O(8)	91.73(16)	91.70
O(4)-V(1)-O3)	149.52(15)	149.58	O(9)-V(2)-O(8)	149.32(15)	149.30
O(1)-V(1)-N3)	107.73(18)	107.78	O(7)-V(2)-N(6)	107.09(17)	107.09
O(2)-V(1)-N3)	142.08(18)	142.00	O(6)-V(2)-N(6)	142.90(18)	142.95
O(4)-V(1)-N3)	82.55(13)	82.69	O(9)-V(2)-N(6)	82.94(14)	82.94(14)
O(3)-V(1)-N3)	73.69(14)	73.69	O(8)-V(2)-N(6)	73.45(14)	73.45(14)
2					

Bond length					
V-O(1)	1.6208(11)	1.6209	V-O(4)	1.9731(10)	1.6209
V-O(2)	1.6465(10)	1.6461	V-N(1)	2.1588(12)	1.6468
V-O(3)	1.9179(10)	1.9175			
Bond angle					
O(1)-V-O(2)	108.96(6)	108.91	O(3)-V-O(4)	144.37(5)	108.90
O(1)-V-O(3)	105.42(5)	105.40	O(1)-V-N(1)	102.75(5)	105.41
O(2)-V-O(3)	96.46(5)	96.41	O(2)-V-N(1)	147.12(5)	96.40
O(1)-V-O(4)	105.29(5)	105.20	O(3)-V-N(1)	83.08(4)	105.25
O(2)-V-O(4)	90.27(5)	90.31	O(4)-V-N(1)	72.90(4)	90.20

Table 6 Hydrogen-bonding interactions [Å and °] for complexes **1** and **2**.

D-H···A	**d(D-H)**	**d(H···A)**	**d(D···A)**	**<(DHA)**	**Symmetry transformations**
1					
C(2)-H(2)···O(7)#1	0.93	2.45	3.366(7)	168.5	#1 -1+X,1+Y, +Z
C(14)-H(14B)···O(2)#2	0.96	2.44	3.229(7)	138.9	#2 1-X,1-Y, -Z
C(16)-H(16)···O(3)#3	0.93	2.63	3.320(7)	131.0	#3 +X, -1+Y, +Z
C(28)-H(28B)···O(6)#4	0.96	2.60	3.283(7)	128.1	#4 2-X,1-Y,1-Z
C(29)-H(29)···N(2)#3	0.93	2.62	3.500(7)	158.6	
C(30)-H(30)···O(1)#2	0.93	2.47	3.254(7)	142.0	
C(31)-H(31)···N(1)#5	0.93	2.35	3.207(7)	153.1	#5 -X,2-Y, -Z
C(32)-H(32)···N(4)#6	0.93	2.36	3.187(7)	148.1	#6 1-X, -Y,1-Z
C(33)-H(33)···O(7)#4	0.93	2.50	3.247(7)	138.0	
C(34)-H(34)···N(5)#7	0.93	2.63	3.527(7)	162.1	#7 +X,1+Y, +Z
N(14)-H(14)···O(6)#8	0.87(5)	1.80(6)	2.667(6)	175(5)	#8 1-X,1-Y,1-Z
N(11)-H(11A)···O(2)#9	1.00(7)	1.70(7)	2.675(6)	163(6)	#9 -X,1-Y, -Z
N(13)-H(13)···O(9)	0.81(8)	2.24(8)	2.904(6)	139(7)	
N(13)-H(13)···O(10)	0.81(8)	2.22(8)	2.921(6)	145(7)	
N(12)-H(12)···O(4)	0.83(7)	2.13(7)	2.896(6)	153(6)	
N(12)-H(12)···O(5)	0.83(7)	2.31(7)	2.959(6)	135(6)	
2					
N(4)-H(3B)...O(2)	0.88	2.13	2.8491(17)	138.1	
N(4)-H(3B)...O(4)	0.88	2.19	2.9653(16)	147.4	
N(5)-H(4B)...O(3)#1	0.88	2.22	2.9497(16)	140.0	#1 -x+1, -y+1, -z+2
N(5)-H(4B)...O(5)#1	0.88	2.12	2.8972(16)	146.3	
C(7)-H(7A)...O(1)#2	0.98	2.65	3.622(2)	173.0	#2 -x+1, -y+2, -z+2
C(17)-H(17A)...N(2)#3	0.95	2.49	3.4327(19)	174.1	#3 -x+1, -y+1, -z+1
C(18)-H(18A)...O(1)#4	0.95	2.62	3.3220(19)	131.1	#4 x, y-1, z
C(19)-H(19A)...O(2)	0.98	2.65	3.298(2)	124.1	
C(19)-H(19B)...N(3)#5	0.98	2.69	3.624(2)	159.3	#5 -x+2, -y+1, -z+1
C(19)-H(19C)...N(3)#6	0.98	2.59	3.271(2)	127.0	#6 x, y, z+1

3.9 Thermal analysis

Thermal decomposition studies of complexes **1** and **2** were carried out in the nitrogen atmosphere at temperatures ranging from 25 to 600 °C to determine their decomposition patterns. Metalloid complexes have been found to be more stable than ligands [94]. Fig. 28 displays the TG graphs of the $[V(O)_2(L)]$ImH **1** and $[V(O)_2(L)]$m-ImH **2** complexes. The decomposition of complexes can be seen in three stages on the thermogram. The decomposition pattern is shown in Scheme 4. In the first step, complexes **1** and **2** lose 3.0% and 10% at 100-250 °C of its weight with separation of methoxy group present in the ligand moiety [95]. In step second, there is 35.3% and 31.6% at 350-400 °C weight loss in **1** and **2** respectively due to removal of Imidazole and 2-methylimidazole. The last step about 19.2 % and 23.8% decomposition of ligand occurs about 19.2% in **1** and 23.8% in **2** at 450-500 °C leaving behind V_2O_5 as the final product.

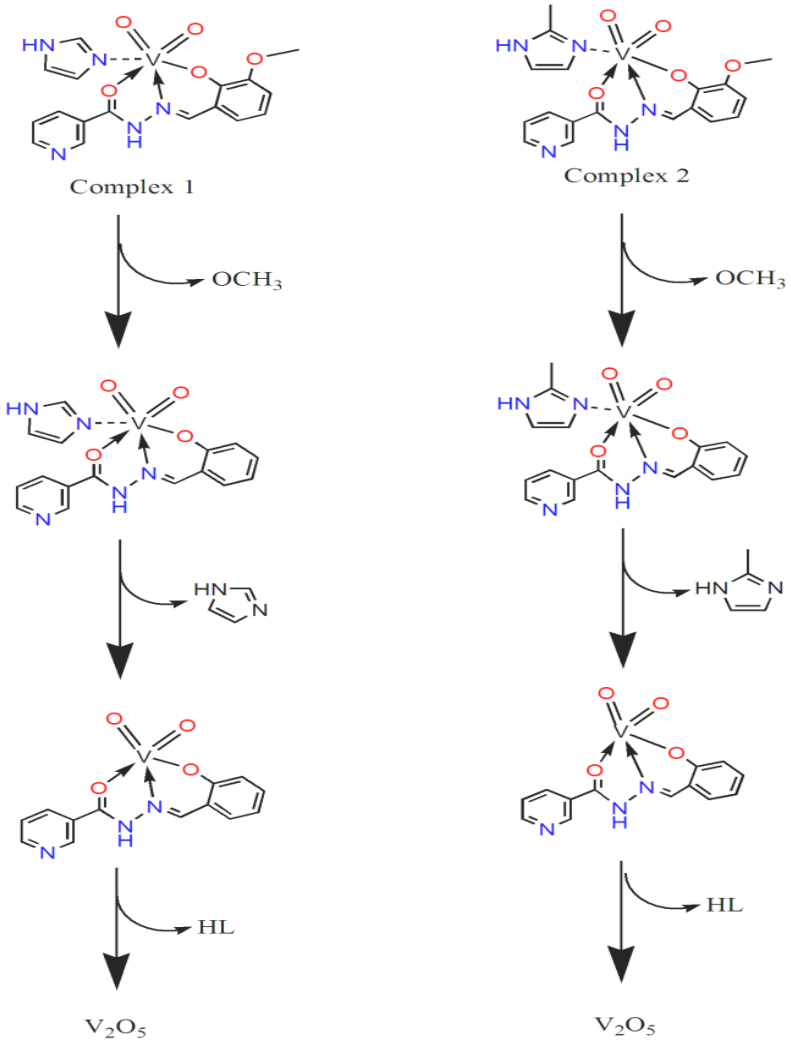

Scheme 4 Schematic diagram for decomposition steps in TGA in complexes **1** and **2**.

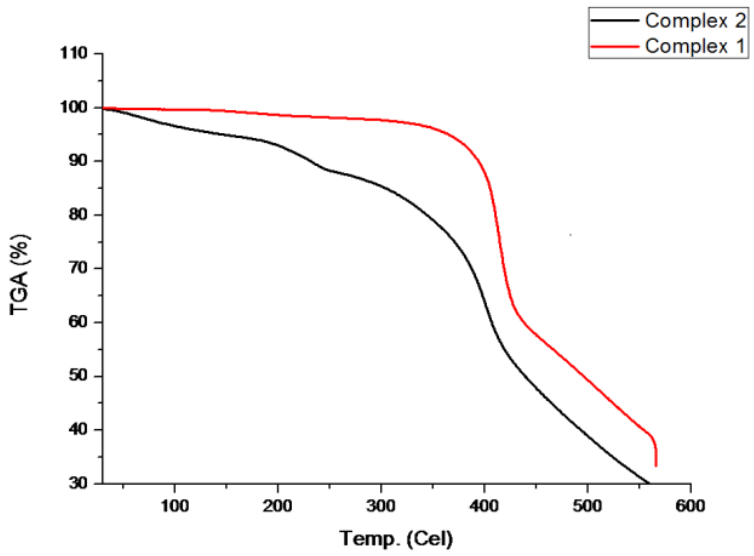

Fig. 28. TGA curves of complex **1** and **2**.

The TGA curve of complexes **3-6** is given in Fig. 29. The decomposition pattern of these complexes is almost similar to that of **1** and **2** complexes. In the TGA graph of these complexes, the first decomposition starts at around ~ 180 °C which due to the removal of the methoxy group from the ligand moiety. The second step decomposition is in-between temperature 350-450 °C which is due to the removal of co-ligand. In the final step, the decomposition of pro-ligand occurs at around ~ 450 °C leaving behind the final product V_2O_5.

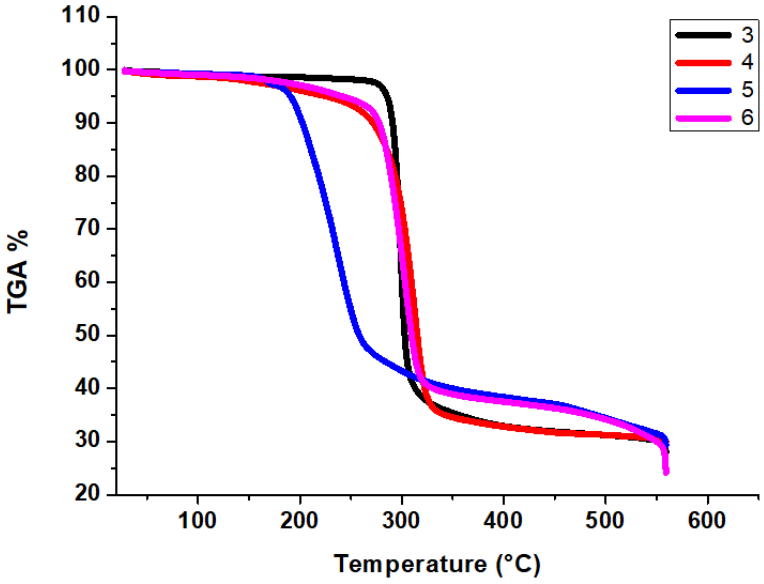

Fig. 29. TGA curves of complexes **3-6**.

3.10 Antidiabetic activity

3.10.1 Antioxidant activity

The result of the *in vitro* antioxidant activity of **H_2L**, **1** and **2** is presented in Table 7. The IC_{50} was calculated for DPPH radical scavenging assay. The IC_{50} values of **H_2L** and complexes **1** and **2** were 729.26, 422.58 and 441.40 µg/ml respectively, whereas that of ascorbic acid was 730.12 µg/mL. The DPPH scavenging activity was lower than that of positive control ascorbic acid, while higher than that of **HL**. Wazalwar and co-workers reported a similar DPPH scavenging activity of vanadium(V) complexes (Fig. 30) [96]. These results showed that the complexes have the potential in scavenging free radicals. Reactive oxygen species (like, O_2^-, H_2O_2 etc.) were major by-products of oxidative metabolism in the mammalian system. These species play a major role in immunity and signal transfer, but species could induce many diseases owing to damaging tissue and cells. Such as cardiovascular diseases, diabetes and Alzheimer's disease. Several studies have confirmed that vanadium complexes could quench scavenging free radicals and protect against diseases [97, 98]

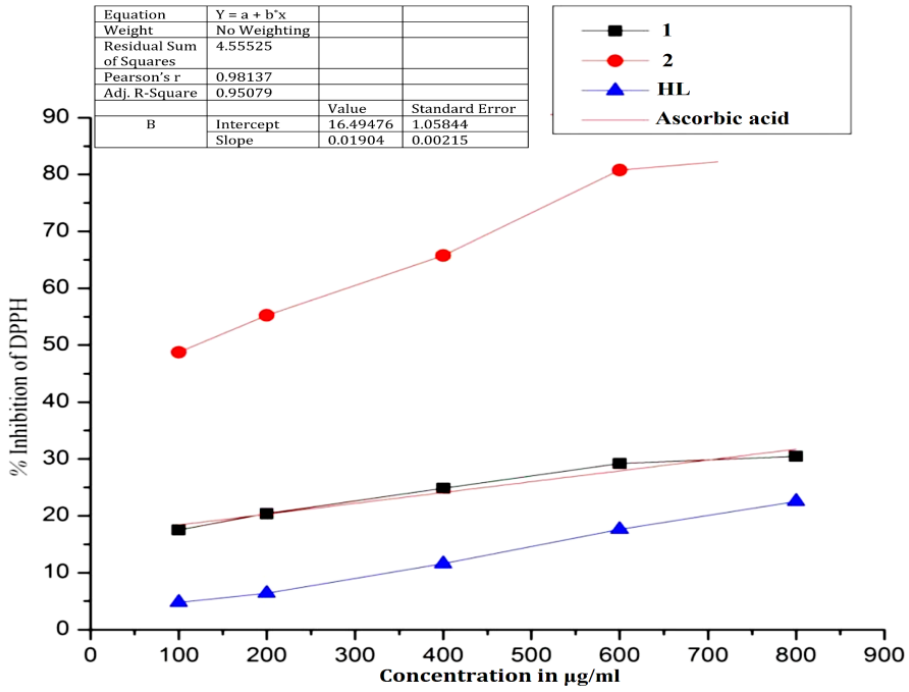

Fig. 30. DPPH antioxidant inhibition of **1**, **2** and **H_2L**.

3.10.2 α-Glucosidase inhibition activity

The Schiff base H_2L and complexes **1** and **2** showed inhibitory activity against α-glucosidase. Following the *in vitro* experiments, the IC_{50} values of H_2L, **1** and **2** were 26.89, 153.03 and 32.54 μg/mL respectively. H_2L and **2** showed low IC_{50} values towards the inhibition of α-glucosidase and these values are similar to that of the control acarbose. These results showed that the H_2L, **1** and **2** complexes were a potent inhibitor against α-glucosidase (Fig. 31). These observations are consistent with the results of reported similar vanadium complexes [99-102].

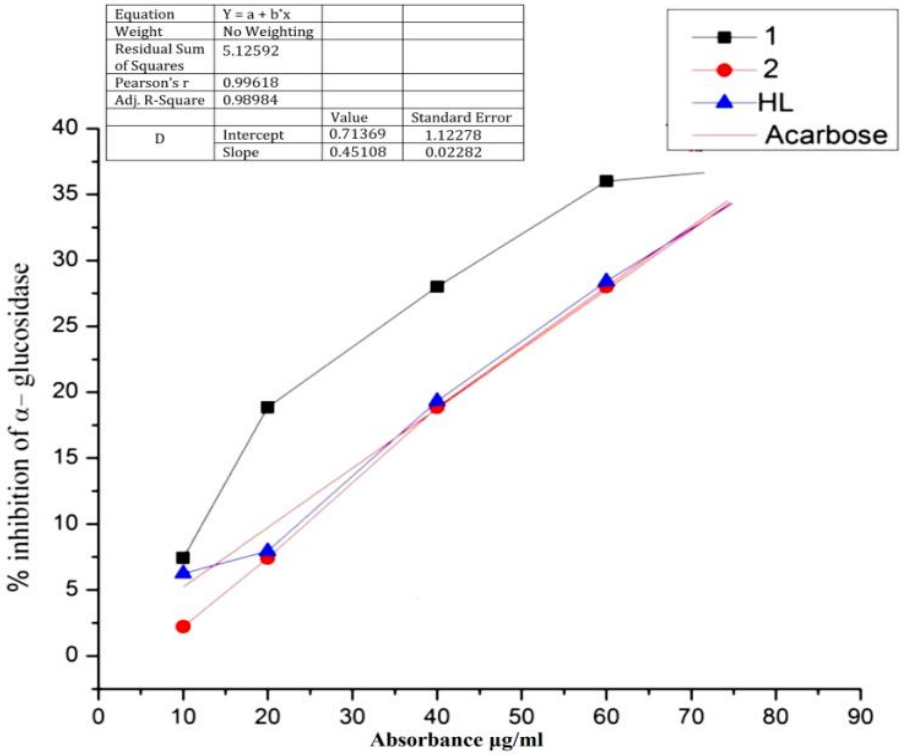

Fig. 31. α-Glucosidase inhibition of **1**, **2** and **H_2L**.

3.10.3 α-Amylase inhibition activity

The α-amylase inhibition activity of the H_2L, **1** and **2** against Acarbose was measured and presented in Table 7. α-amylase plays a major role in the hydrolysis of starch to maltose. Hence, the inhibition of α-amylase is a strategy for the management of diseases such as diabetes and obesity. Found lowest IC_{50} value is 23.67 in **1** (23.669 ± 15.07) while the highest IC_{50} in **2** (182.901 ± 285.3) and moderate in H_2L IC_{50} (56.7959 ± 14.58). It was

thus revealed that complex **1** showed the highest *in vitro* α-amylase (insulin-mimetic) activity among compounds examined in this study (Fig. 32). Therefore, here we can conclude that all samples give remarkable α-amylase inhibition and showed concentration-dependent activities. These findings were similar to the results of Tripathi and co-workers [103].

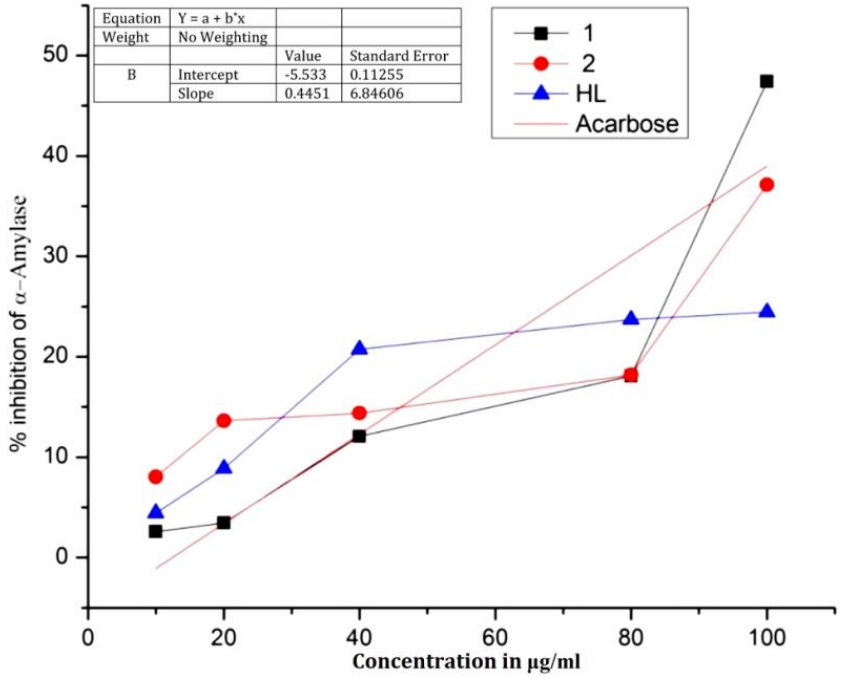

Fig. 32. α-Amylase inhibition of **1**, **2** and **H_2L**.

3.10.4 β-Glucosidase inhibition activity

This is an important finding because sweet almonds have β-glucosidase. Hence, these compounds have a positive effect on the sweet almonds β-glucosidase similar to the reported findings of vanadyl complexes [104]. The β-glucosidase inhibitory activity of H_2L, **1** and **2** were investing ahead of and presented in Table 7. The IC_{50} value of β- glucosidase inhibition was found lowest in sample H_2L (19.5252 ± 13.44) while highest in 2 (2021.77 ± 5.547) and moderate in complex **1** (282.05 ± 1.284). Therefore, here we can conclude that all samples give good inhibition and showed concentration-dependent activities (Fig. 33).

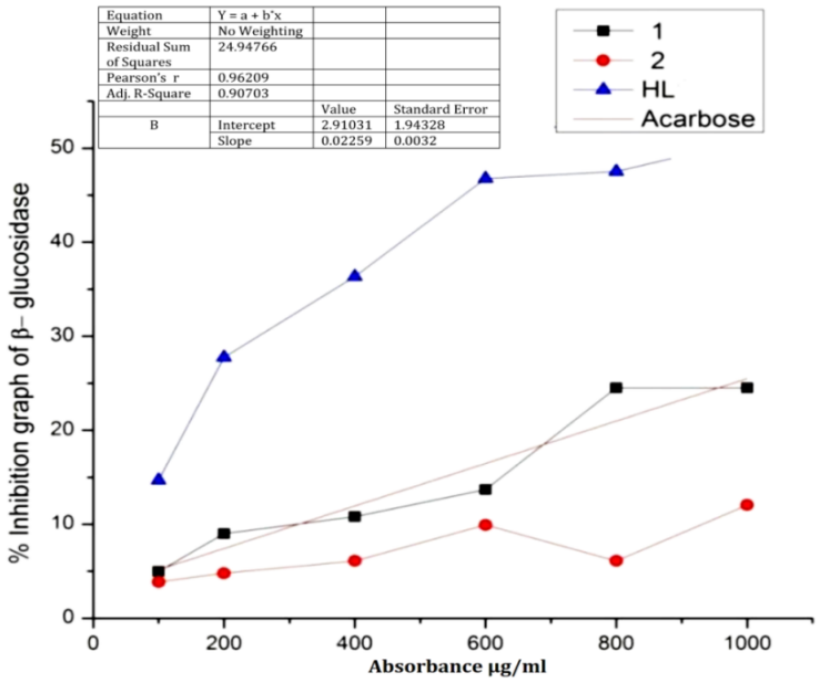

Fig. 33. β-Glucosidase inhibition of **1**, **2** and **H_2L**.

Table 7 IC_{50} Values of compounds in different activities.

S. No.	Activity	1	2	H_2L
1	DPPH	422.579 ± 0.011	441.396 ± 0.075	729.258 ± 0.001
2	α-Glucosidase	153.037 ± 0.005	32.542 ± 0.037	26.888 ± 0.007
3	α-Amylase	23.669 ± 0.001	182.901 ± 0.028	56.796 ± 0.008
4	β-Glucosidase	282.050 ± 0.005	2021.770 ± 0.005	19.525 ± 0.005

3.10.5 α-Glucosidase inhibition activity

The % inhibition of α-glucosidase enzyme activity of complexes **3-6** was determined by the previously reported method [103]. The % inhibition plots are shown in Fig 34. and IC_{50} values and α-glucosidase activity parameters are listed in Table 8. The IC_{50} values of each complex were determined from the inhibition plot between % inhibition *vs.* concentrations. The concentration-dependent activity of α-glucosidase was observed in all complexes. Although the IC_{50} of present complexes is less than the control acarbose (standard). The observed trend in is: **4** > **3** > **6** > **5**. The geometry of present complexes is distorted square planar, these may be α-glucosidase at the active site. After the association of α-glucosidase in the vacant coordination site of vanadium(V), the establishment of hydrogen bonding and hydrophobic interactions may cooperatively stabilize the inhibitor [105]. Additionally, the mode of inhibition was monitored for complex with the best inhibition

activity and it showed the mixed-type inhibition. These complexes might be potent antidiabetic agent and used as a candidate for treating diabetes or food additive capable of delaying carbohydrate digestion.

Table 8 α-Glucosidase inhibition activity of **3-6**.

Compound	IC_{50} (µg/mL)	α-glucosidase activity ($µg^{-1}$)
3	50.23	19.91
4	32.48	30.69
5	64.17	15.58
6	59.88	16.70

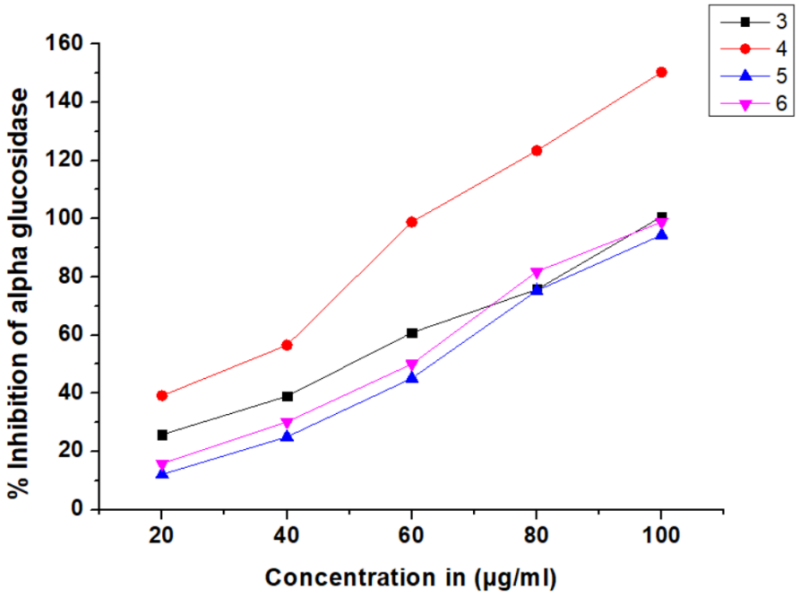

Fig. 34. α-Glucosidase inhibition activity of complexes **3-6**.

3.10.6 α-Amylase inhibition activity

The inhibition study of the α-amylase digestive enzyme was also performed using the reported method [106]. This enzyme converts the insoluble starch into glucose and is considered one of the most targets in the treatment of diabetes and hyperlipidaemia [107]. The evaluated IC_{50} values and α-amylase activity are listed in Table 9. The inhibition plots are shown in Fig 35. These complexes showed the trends of IC_{50} similar to the trend observed for α-amylase activity measurements. Complex **3** revealed the highest amylase activity. This complex is the softest and the smallest ΔE being most active. The present complexes have shown better inhibition activity against the α-amylase enzyme. The distorted square

pyramidal geometry of the complexes may bind the active site through hydrogen bonding or other hydrophobic interactions. Therefore, block the access active site of the enzyme or changes of chemical environment around it due to allosteric interactions. Thus, the enzyme is no longer active for the hydrolysis of the starch into glucose [108].

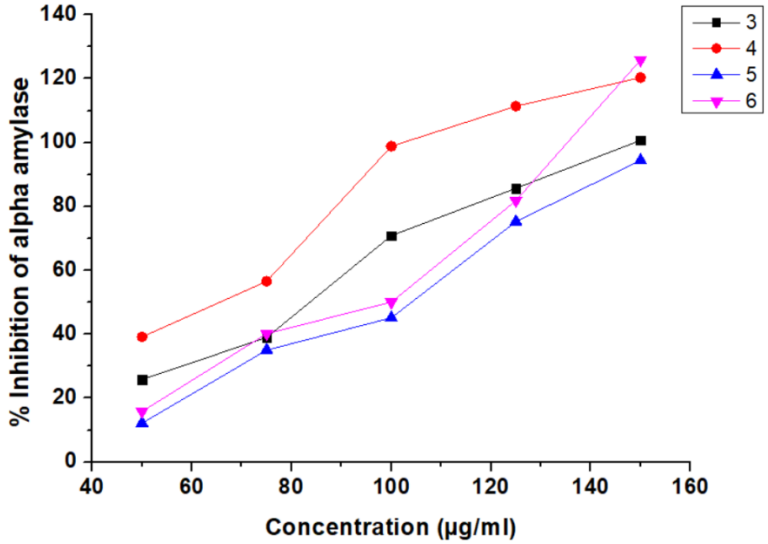

Fig. 35. α-Amylase inhibition of **3-6.**

Table 9 α-Amylase inhibition activity of complexes **3-6.**

Compound	IC_{50} (µg/mL)	α-amylase activity ($µg^{-1}$)
3	84.33	11.85
4	64.68	15.46
5	105.47	9.48
6	100.97	9.90

3.11 Hirshfeld Surface Analysis (HSA)

Molecular Hirshfeld surfaces [109] in the crystal structure were constructed based on the electron distribution calculated as the sum of spherical atom electron densities [110, 111]. For a given crystal structure and a set of spherical atomic densities, the Hirshfeld surface is unique [112]. The normalized contact distance (d_{norm}) based on both d_e and d_i (where d_e is the distance from a point on the surface to the nearest nucleus outside the surface and d_i is the distance from a point on the surface to the nearest nucleus inside the surface) and the vdW radii of the atom, as given by eq 1 enables identification of the regions of particular importance to intermolecular interactions. The combination of d_e and d_i in the form of a two-

dimensional (2D) fingerprint plot [113, 114]. Provide a summary of intermolecular contacts in the crystal [109]. The Hirshfeld surfaces mapped with d_{norm} and 2D fingerprint plots were generated using the Crystal-Explorer 2.1 [115]. Graphical plots of the molecular Hirshfeld surfaces mapped with d_{norm} used a red-white-blue colour scheme, where red highlights shorter contacts, white represents the contact around vdW separation, and blue is for longer contact. Additionally, two further coloured plots representing shape index and curvedness based on local curvatures are also presented in this paper [116].

$$d_{norm} = \frac{d_i - r_i^{vdW}}{r_i^{vdW}} + \frac{d_e - r_e^{vdW}}{r_e^{vdW}} \quad ...(1)$$

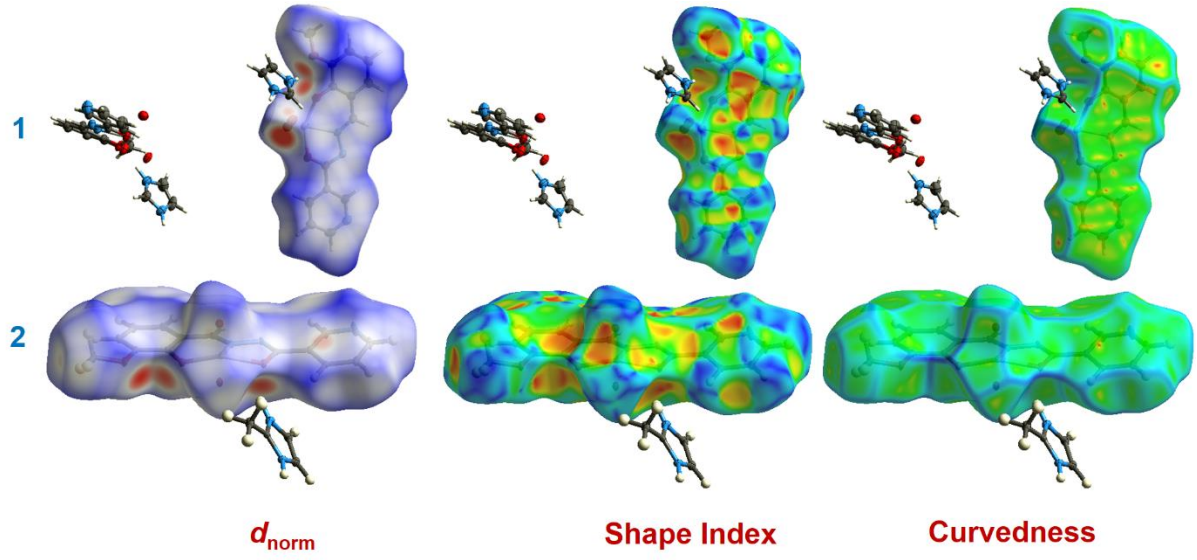

Fig. 36. Hirshfeld surfaces mapped with d_{norm}, shape index and curvedness for complexes **1** and **2**.

The Hirshfeld surfaces for both complexes are presented in Fig. 36. For better visualization of the molecule, these surfaces are plotted as transparent. The d_{norm} surface for both the complexes are mapped between -0.35 to 1.25 Å range, shape index plots are constructed between -1.0 to 1.0 Å while curvedness plots are mapped in the range -3.5 to 0.35 Å. In **1**, the O···H and NH···π interactions and in **2** the CH···π interactions as discussed for both the complexes in the crystallographic section (vide supra) can be seen as the large circular deep red depressions. The relatively weaker V···O interaction in **1** and

O···πinteractions in **2** can be seen as the faint red shaded area in the corresponding d_{norm} surfaces Fig. 37.

Another very relevant result of the Hirshfeld surface is the fingerprint plot analyses (Fig. 37). In these 2D plots, the complementary regions are presented in such a mode where one molecule act as donor ($d_e > d_i$) and another as an acceptor ($d_e < d_i$). Additionally, the total fingerprint plots could be cleaved into several layers to put stress on the particular atom pair close contacts. Such plots enable the estimation of contributions coming from various interactions existing in the molecule. The fingerprint plots of both the complexes display a light blue region which represents various interactions existing in the complex (*vide infra*). In **1**, the most important interaction in the ligand is the O···H/H···O interaction which appears as discrete spikes 1.0 Å < (d_e + d_i) < 2.3 Å in the total fingerprint plot and has a contribution of 30%. Besides, NH···π/π···HN interaction, as well as V···O interactions, also exist in **1** which contributes 15.0% and 2.2% in the total fingerprint plot. In **2**, the most important is the C-H···π appearing as blunt spikes in the region 1.1 Å < (d_e + d_i) < 2.3 Å and contributes 18.8% in the total Hirshfeld surface area of the complex. Apart from this the complex also exhibits O···π interactions appearing between in 1.4 Å < (d_e + d_i) < 2.3 Å with an overall contribution of 2.3% in the total fingerprint plot of **2**.

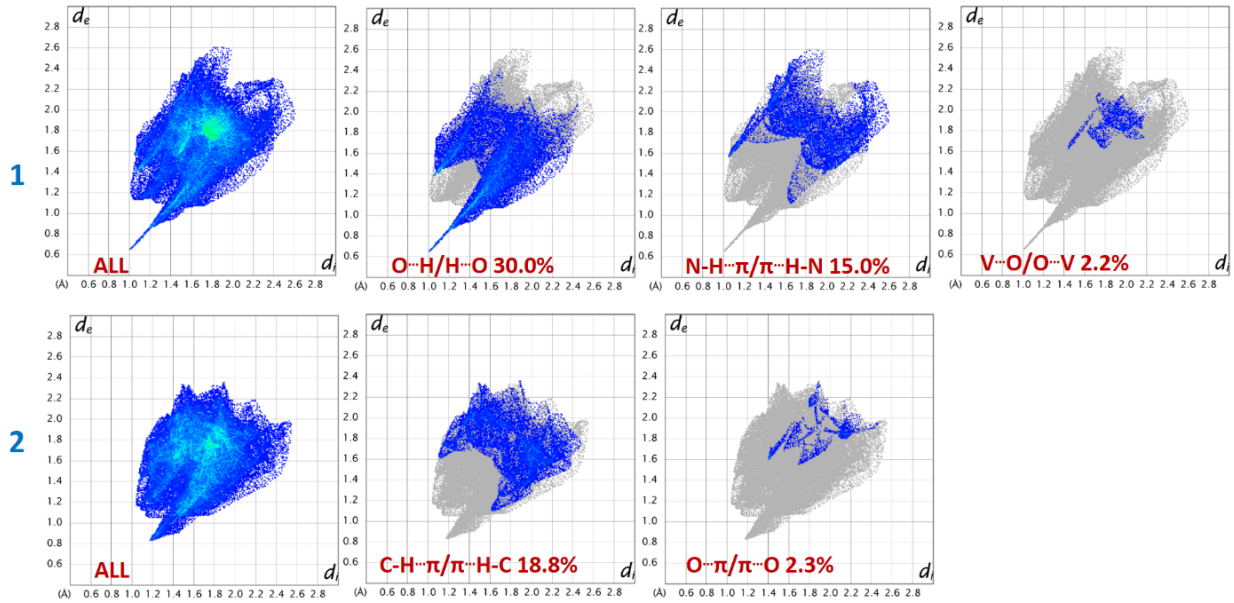

Fig. 37. Fingerprint plots for the ligand showing percentages of contact contributed to the total Hirshfeld surface area in the complexes **1** and **2**.

3.12 Computational studies of complexes

The electronic structure of complex **1** and **2** correlating the experimental bond distances and angles was investigated by the DFT calculations using B3LYP functional. The optimized structure of complex **1** and **2** is shown in Fig. 38. The experimental single-crystal X-ray analysis data bond distances and angles are in good agreement with calculated data. However, some bond distances and angles deviate significantly from those obtained from the single-crystal X-ray diffraction data. The difference in data is an expected result because geometrical optimizations are performed in the gaseous state in which intermolecular interactions are absent. The optimized molecular structure is more extended compared to experimental X-ray diffraction data calculated in solid state in which significant intermolecular interactions become prominent. Analysis of the frontier molecular orbitals of the gas phase optimized geometry of complex have been substantiated that the frontier highest occupied molecular orbitals (HOMO) and the lowest unoccupied molecular orbitals (LUMO) of **1** are mainly constituted of vanadium *d*- and HL orbitals. Counter plots of some selected molecular orbitals and the energy gaps in between two energy levels are shown in Fig. 39. The observed trend in energy gaps in α- and β- the spin state is:

HOMO-2 – LUMO+2 > HOMO-1 – LUMO+1 > HOMO-LUMO

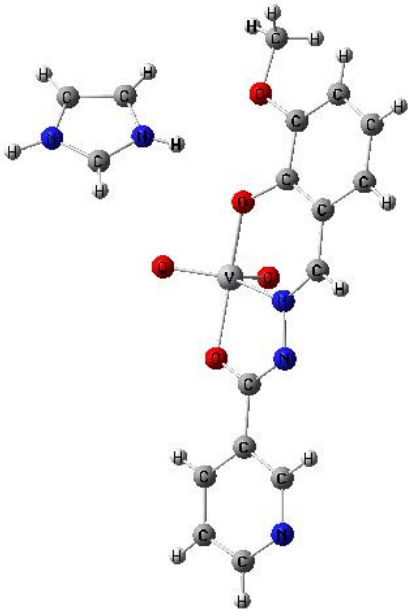	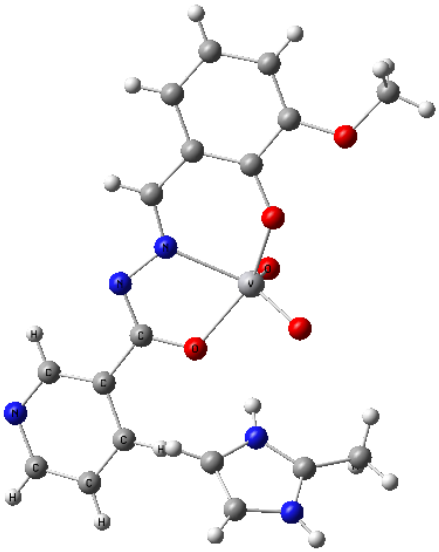
1	**2**

Fig. 38. Optimized structure of complex **1** and **2**.

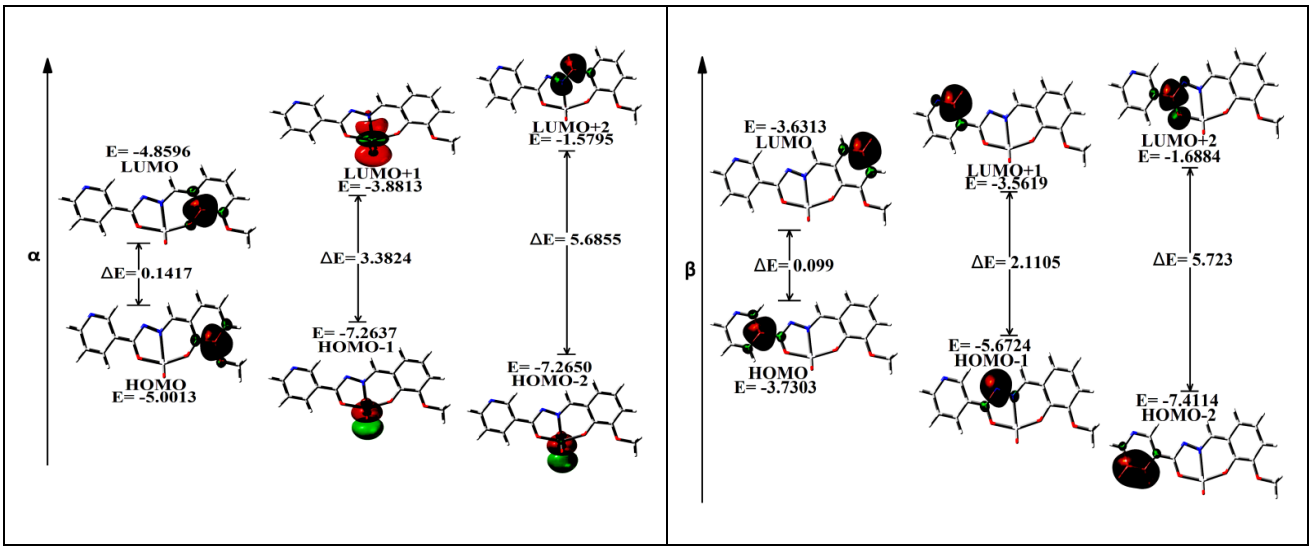

Fig. 39. HOMO-LUMO energies and energy gap of complex **1**.

3.12.1 Mulliken spin population analysis

Mulliken spin population analysis is also performed to determine the partial atomic charges [117]. These charges yield important information about the origin of molecular properties including dipole moments and molecular polarizability. Although, it has been used to describe the electrostatic potential surfaces in molecular structure [118, 119]. Mulliken spin population of **1** is shown in Fig. 40. In the spin density plot green lobes show positive spin density whereas blue lobes show negative spin density. The DFT calculated atomic Mulliken charges are collected in Table 10. From Table 10, it is clear that all oxygen atoms carry high negative charges, V atom carries the highest positive charge. Nitrogen atoms also carry moderate negative charges, while on C atoms remain both positive and negative charges.

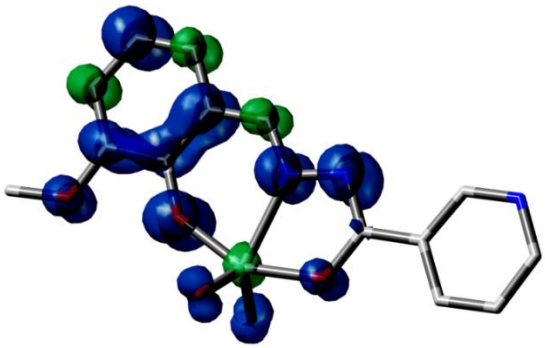

Fig. 40. Calculated spin-density distribution for the ground state (S = ½) of **1** with a surface threshold level of 0.004.

Table 10 Mulliken spin population data of complex **1**.

Atom No.	Charges	Atom No.	Charges
C6	0.231	O1	-0.364
C7	-0.264	O2	-0.364
C8	0.372	O3	-0.420
C9	-0.360	O4	-0.368
C10	-0.200	O5	-0.241
C11	-0.327	N1	-0.009
C12	0.249	N2	-0.148
C13	0.163	N3	-0.266
		V	0.907

3.12.2 Geometrical optimization

The geometry of complexes **3-6** has been optimized at the B3LYP level of the theory [120]. In this method, 6-31G(d) basis set for C, H, N and O and LANN2DZ for vanadium metal were used to access reliable results of the experimental values. This theory permits a quantitative discussion of molecular structures but also the ground electronic properties of the investigated compounds. Geometric features of complexes were calculated by optimization of their bond angles and bond lengths. The optimized geometry of complexes **3-6**with atom numbering are shown in Fig. 41-44. and bond parameters are collected in Table.11. Also, their calculated quantum chemical parameters (crucial electronic parameters) are shown in Table 11. The coordination sphere in each complex around the vanadium metal centre is distorted square pyramidal. The extent of distortion was calculated using Addison structural parameter (τ_5). Its value can be calculated using equation

$$\tau_5 = \theta_1\text{-}\theta_2/60$$

where θ_1 and θ_2 are the largest bond angles. The value of τ_5= 1 for perfect trigonal pyramidal and τ_5= 0 is for perfect square pyramidal. The values of τ5 for present complexes are in the range 0.005-0.098. Therefore, the geometry of vanadium in these complexes is very close to square-pyramidal with minor distortion in geometry. The bond lengths of vanadium to donor atoms of tridentate Schiff base are in the range found for other reported complexes having the dioxidovanadium(V) moiety [121, 122].

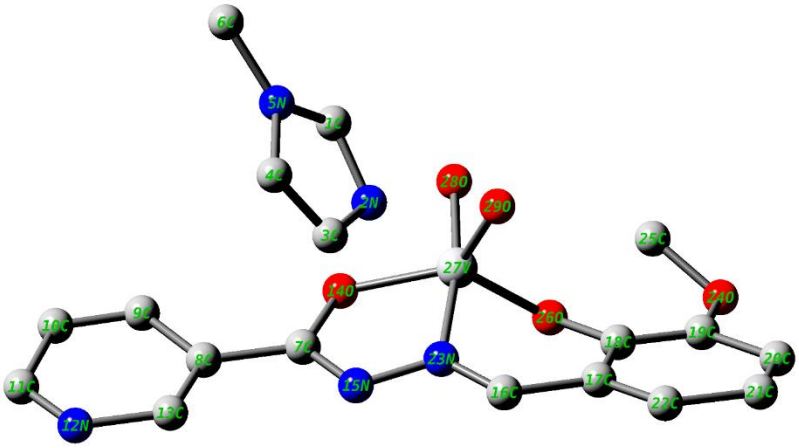

Fig. 41. Optimized structure of complex **3**.

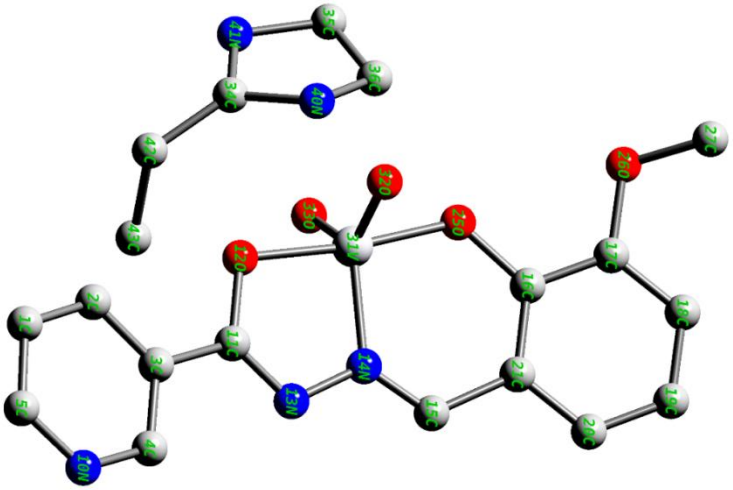

Fig. 42. Optimized structure of complex **4**.

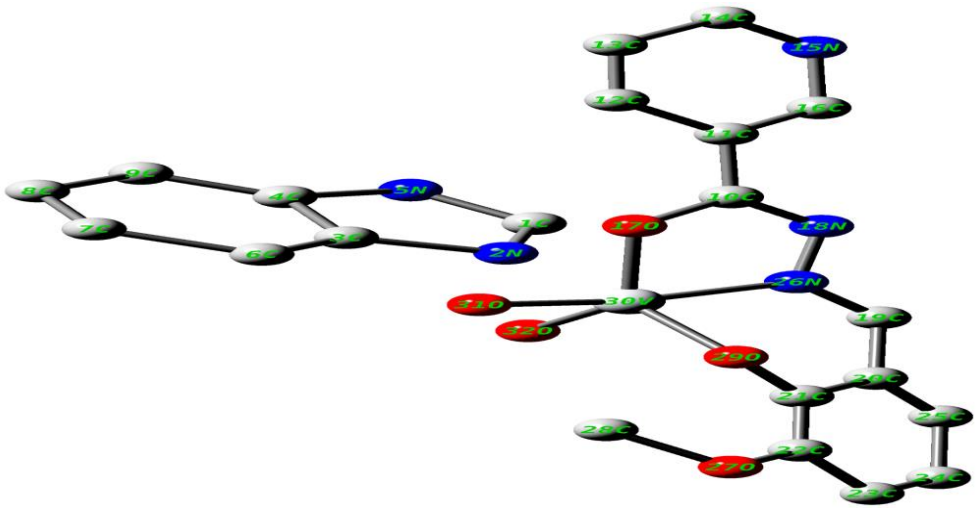

Fig. 43. Optimized structure of complex **5**.

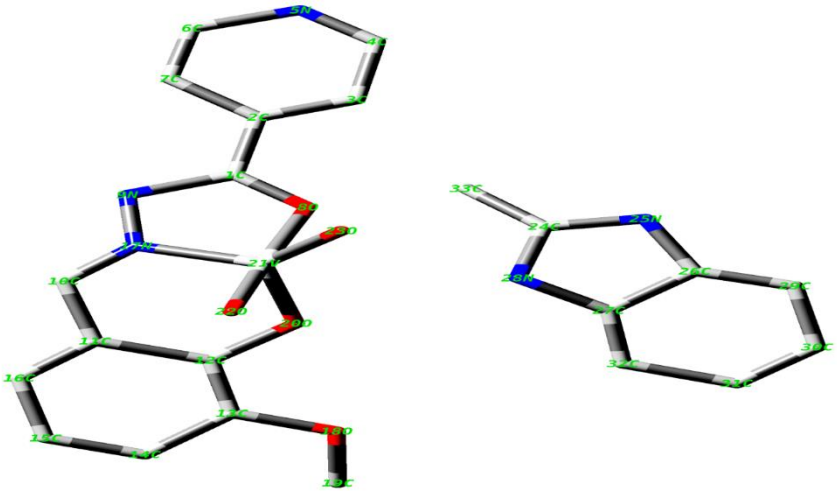

Fig. 44. Optimized structure of complexes **6**.

Table 11 Theoretical Bond lengths [Å] and angles [°] for complexes **3-6**

3		4		5		6	
Bond length							
V(27)-O(14)	1.870	V(31)-O(32)	1.636	V(30)-O(31)	1.636	V(21)-O(8)	1.863
V(27)-O(26)	1.859	V(31)-O(33)	1.636	V(30)-O(32)	1.636	V(21)-O(20)	1.837
V(27)-O(28)	1.852	V(31)-O(25)	1.863	V(30)-O(29)	1.856	V(21)-O(22)	1.860
V(27)-O(29)	1.870	V(31)-O(12)	1.870	V(30)-O(17)	1.881	V(21)-O(23)	1.859
V(27)-N(23)	1.897	V(31)-N(14)	1.879	V(30)-N(26)	1.892	V(21)-N(17)	1.858
Bond angles							
O(14)-V(27)-N(23)	82.05	O(12)-V(31)-N(14)	85.12	O(17)-V(30)-N(26)	82.85	O(8)-V(21)-N(17)	82.57
O(14)-V(27)-O(26)	125.53	O(12)-V(31)-O(32)	92.92	O(17)-V(30)-O(29)	126.34	O(8)-V(21)-O(20)	103.48

O(14)-V(27)-O(28)	108.64	O(12)-V(31)-O(33)	88.97	O(17)-V(30)-O(31)	85.96	O(8)-V(21)-O(23)	85.60
O(14)-V(27)-O(29)	97.94	O(12)-V(31)-O(25)	120.16	O(17)-V(30)-O(32)	127.57	N(17)-V(21)-O(20)	100.64
N(23)-V(27)-O(26)	97.81	N(14)-V(31)-O(25)	102.05	N(26)-V(30)-O(29)	96.24	N(17)-V(21)-O(22)	103.62
N(23)-V(27)-O(28)	89.47	N(14)-V(31)-O(32)	113.70	N(26)-V(30)-O(32)	92.37	N(17)-V(21)-O(23)	131.13
O(26)-V(27)-O(28)	125.81	O(25)-V(31)-O(32)	87.71	O(29)-V(30)-O(31)	91.77	O(20)-V(21)-O(22)	85.31
O(26)-V(27)-O(29)	82.18	O(25)-V(31)-O(33)	84.12	O(29)-V(30)-O(32)	106.07	O(20)-V(21)-O(23)	128.22
O(28)-V(27)-O(29)	90.52	O(32)-V(31)-O(33)	126.05	O(31)-V(30)-O(32)	93.06	O(22)-V(21)-O(23)	82.84

3.12.3 HOMO-LUMO Analysis

The HOMO-LUMO analysis of complexes **3-6** were carried out. The frontier molecular orbitals (FMO) highest occupied molecular orbital (HOMO) and lowest unoccupied molecular orbital (LUMO), can be applied to discuss electron donors and acceptors, which control the bioactivity and decide the way a molecule interacts with the biological systems [123,124]. The investigation on their frontier molecular orbitals can reveal useful information for the working mechanism of the bioactive compounds, such as active sites [125,126]. The investigated frontier molecular orbitals (symmetrically placed) are shown in Fig. 45-48. The HOMO, HOMO-1, HOMO-2, and HOMO-3 of **3** are localized predominantly on tridentate Schiff base ligand whereas LUMO, LUMO+1 and LUMO+2 are localized predominantly except on LUMO+3 on vanadium(V) center with methyl imidazolium moiety Fig. 45. In complex **4**, the major contribution is on the tridentate Schiff base ligand of this complex. Only HOMO-2 and LUMO+2 orbitals are localized on the ethyl moiety of counter imidazolium ion (Fig. 46). In complex **5**, HOMO and HOMO-1 is localized on both vanadium and oxygen atoms of VO_2^+ moiety. HOMO-2 and HOMO-3 are exclusively located on benzimidazolium counter ion Fig. 47. LUMO, LUMO+1 and LUMO+3 is on both tridentate ligand and benzimidazolium ion. In complex **6**, HOMO is mainly confined to one oxygen atom of VO_2^+ moiety and HOMO-1, HOMO-2 and HOMO-3 are limited on methyl benzimidazolium moiety Fig. 48. Similarly, LUMO and LUMO+1 are confined on the tridentate ligand and the rest LUMO+2, and LUMO+3 are composed of

oxygen atoms of VO_2^+, vanadium metal and donor atoms of tridentate Schiff base. The HOMO-LUMO analysis suggests that the vanadium cation and tridentate Schiff base may be the reactive sites of these complexes.

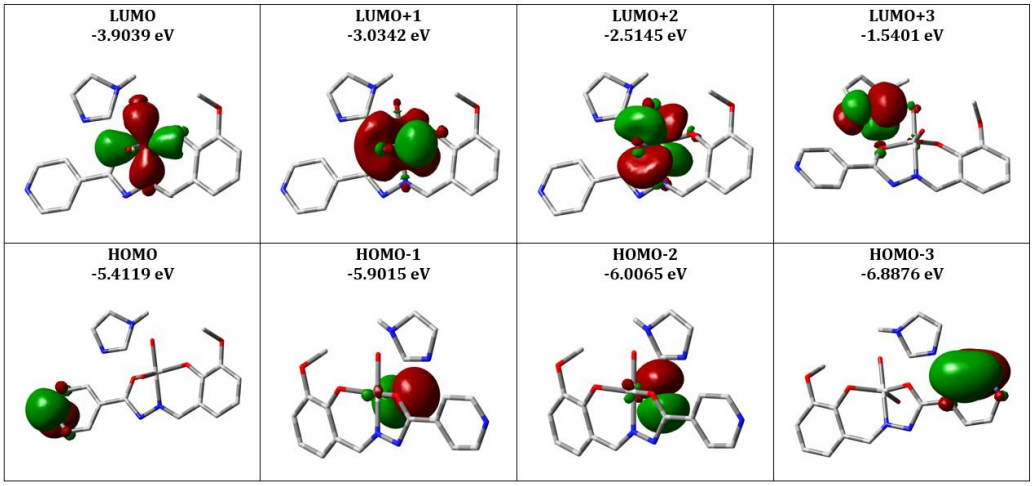

Fig. 45. HOMO-LUMO analysis of **3**.

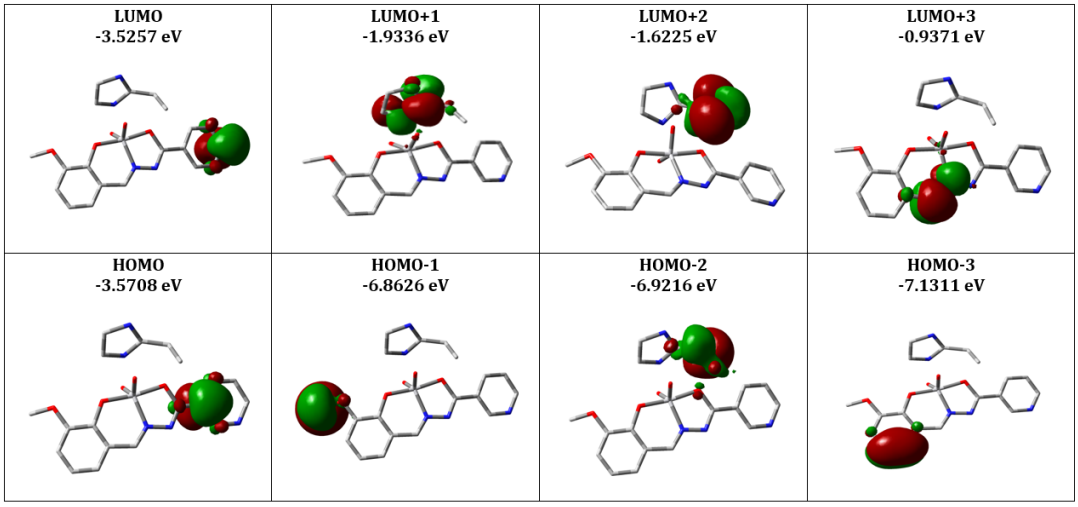

Fig. 46. HOMO-LUMO analysis of **4**.

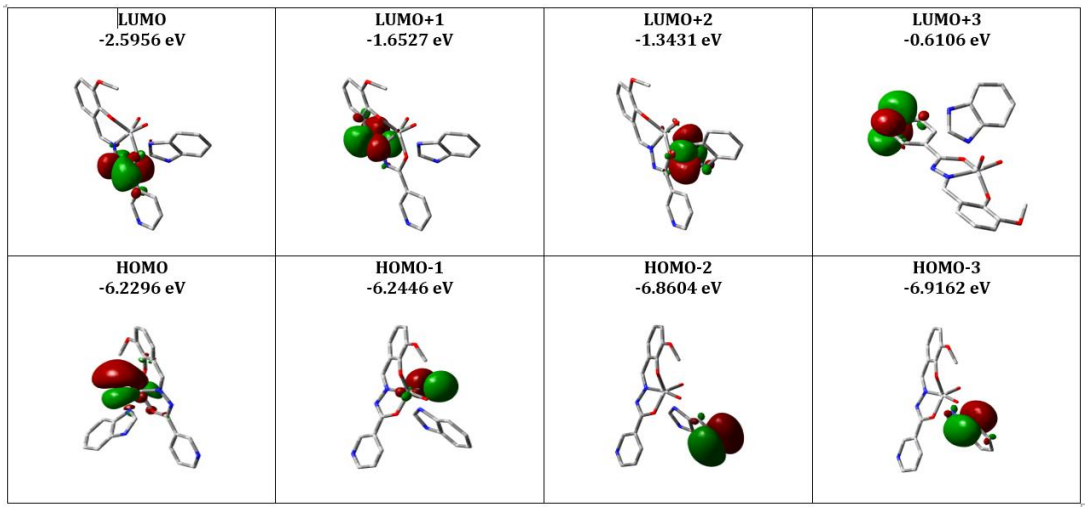

Fig. 47. HOMO-LUMO analysis of **5**.

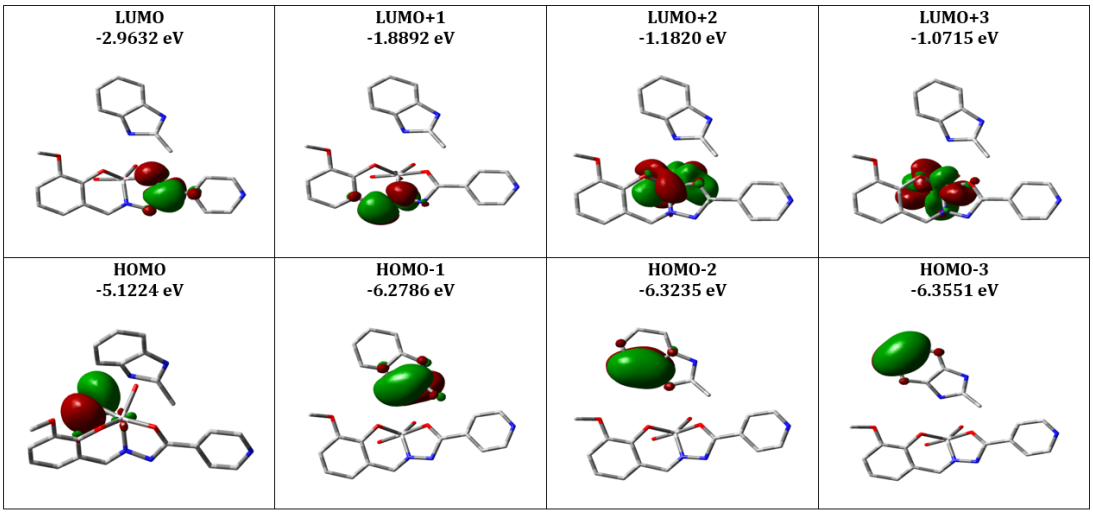

Fig. 48. HOMO-LUMO analysis of **6**.

3.12.4 Mulliken charges analysis

The atomic charge population of a compound is related to the active site in its electrophilic or nucleophilic reactions and the charge interaction between two molecules [125]. Spin density plots are also shown in Fig. 49-52. A considerable amount of spin distribution is into the coordinated atoms. The Mulliken atomic charges of vanadium complexes **3-6**were obtained employing Mulliken population analysis and are listed in Table. 12. On perusal of Mulliken population analysis, it is obvious that the coordination leads to the redistribution of electron density in tridentate Schiff base O atom of VO_2^+ moiety coordinated with vanadium(V). The polarization of complex molecules decreases due electron transfer [127]. The centre vanadium(V) gain electrons to show positive charges of 0.6261 e^- for **3**,

0.8206 $e^-$for **4**, 0.7293$e^-$for **5** and 0.7040 $e^-$for **6**. The decrease in polarity at atoms in complexes is helpful to enhance the bioactivities because the reduction of the polarity of atoms is responsible for enhanced penetration complexes into the lipid membranes [128-130].

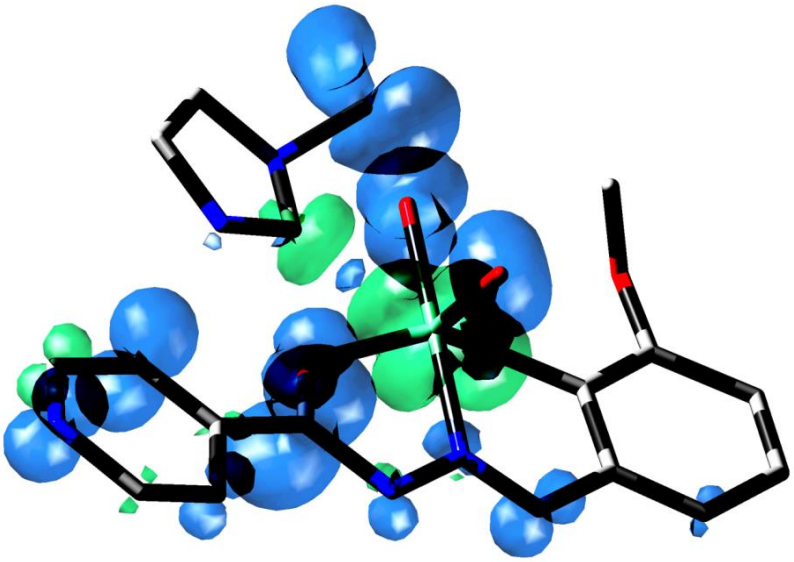

Fig. 49. Spin density plot of complex **3**.

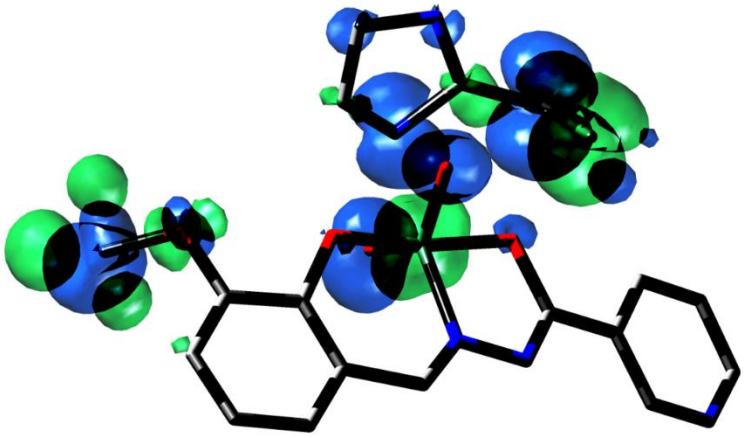

Fig. 50. Spin density plot of complex **4**.

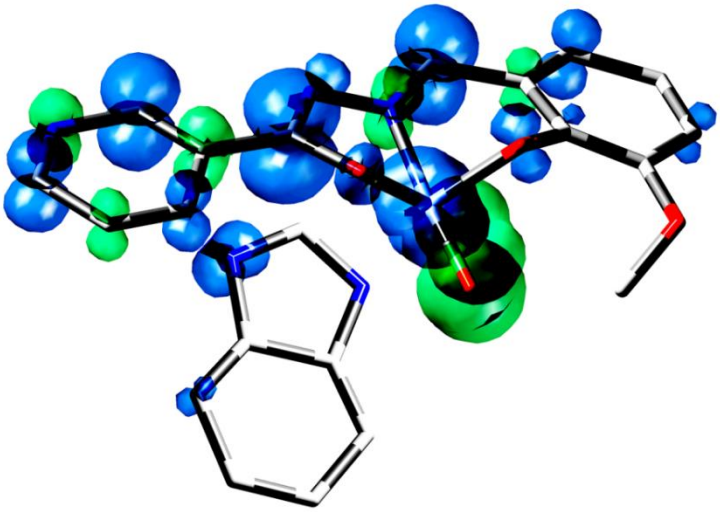

Fig. 51. Spin density plot of complex **5**.

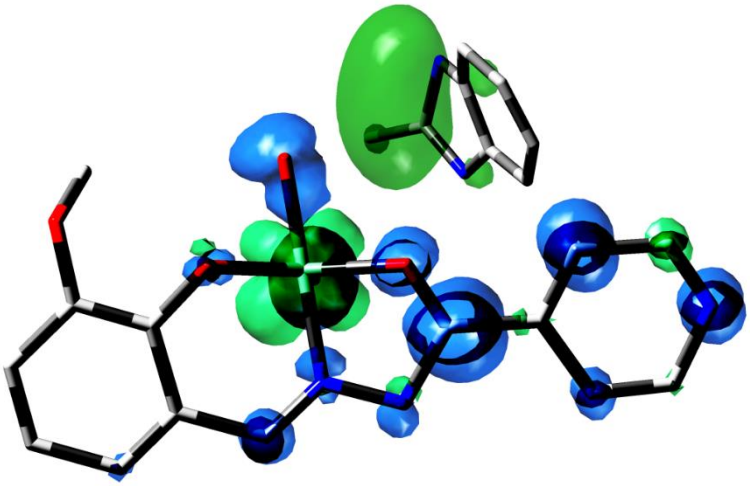

Fig. 52. Spin density plot of complex **6**.

Table 16 The Mulliken densities and charges of metal and donor atoms for complexes **3-6**.

Complexes	Metal and Donor atom	Mulliken charges	Mulliken densities
3	V27	0.7040	-1.0298
	N23	-0.1516	0.0017
	O14	-0.5442	0.0791
	O26	-0.4786	0.0222
	O28	-0.4675	0.2780
	O29	-0.6128	0.3827
	V31	0.6216	-0.3971
	N14	-0.2515	0.0034

4	O12	-0.4978	0.0133
	O25	-0.5026	0.0057
	O32	-0.2788	0.5004
	O33	-0.3985	0.3496
5	V30	0.8206	-0.6600
	N26	-0.1358	0.1244
	O17	-0.2803	0.3595
	O29	-0.4907	0.5138
	O31	-0.4869	0.4001
	O32	-0.3716	0.4325
6	V21	0.7293	-1.1372
	N17	-0.2616	0.0165
	O8	-0.4708	0.1834
	O20	-0.4385	0.0298
	O22	-0.3746	0.1963
	O23	-0.3876	0.1463

3.12.5 Quantitative structure-activity relationship (QSAR)

Associated quantum chemical (crucial electronic) parameters of present complexes were also calculated. These parameters are summarized in Table 13. The objective of the present structure-activity relationship study is to correlate the biological activities of complexes with the most effective quantum chemical molecular descriptors.

The analysis of results of crucial electronic parameters shows that the hardness decreases and softness increase following this trend: **5**, **6**, **3** and **4** which reveals that the charge transfer process is more predominant in **5** compared to other complexes. The magnitude of global hardness(η) supported by ΔE reveals their global hardness signifying the resistance toward the deformation of the electron of a cloud of molecules under small perturbation and is less polarizable. The negative chemical potential of present complexes is suggestive of their stability against that these not undergo decomposition into their respective elements. The observed value of μ and ω show that the **4** is more electrophilic than the others. On contrary, complex **5** is found to be the least electrophilic. Moreover, the value of the electrophilicity index indicates that complex **5** is better nucleophilic than remaining complexes. Thus, the **3** and **4** are the most reactive towards nucleophilic and electrophilic attacks, respectively.

Table 13 The crucial electronic parameters for complexes **3**-**6**.

Molecular Descriptor	Mathematical description	3	4	5	6
E_{HOMO} (eV)	Energy of HOMO	-5.4119	-3.5708	-6.2296	-5.1224
E_{LUMO} (eV)	Energy of LUMO	-3.9039	-3.5257	-2.5956	-2.9632
Energy gap (eV)	$\Delta E = E_{HOMO} - E_{LUMO}$	1.508	0.0451	3.6340	2.1592
Ionization potential (eV)	$I = - E_{HOMO}$	5.4119	3.5257	6.2296	5.1224
Electron affinity (eV)	$EA = - E_{LUMO}$	3.9039	3.5257	2.5956	2.9632
Electronegativity (eV)	$\chi = (I+EA)/2$	4.6579	3.5482	4.4126	4.0428
Chemical potential (eV)	$\mu = - \chi$	-4.6579	-3.5482	-4.4126	-4.0428
Global hardness (eV)	$\eta = (I-EA)/2$	0.7540	0.0225	1.8170	1.0796
Softness (eV^{-1})	$S = 1/2\eta$	0.6631	22.2212	0.2752	0.4631
Electrophilicity index	$\omega = \mu^2/2\eta$	14.3873	279.77	5.3580	7.5696
Electron donating capacity	$\omega- = (3E_{HOMO} + E_{LUMO})^2 / 16(E_{HOMO} - E_{LUMO})$	16.8105	280.9361	7.7914	10.051
Electron accepting capacity	$\omega+ = (E_{HOMO} - 3E_{LUMO})^2 / 16(E_{HOMO} - E_{LUMO})$	12.1526	277.3878	3.3788	5.6831

4 Conclusions

Schiff base ligand H_2L N'-(2-hydroxy-3-methoxybenzylidene) nicotinohydrazide have been prepared and characterized by FTIR, ^1H and ^{13}C NMR. In this work, six oxidovanadium(V) complexes of tridentate Schiff base ligand H_2L N'-(2-hydroxy-3-methoxybenzylidene) nicotinohydrazide having donor site ONO was synthesized and characterized by a various physico-chemical and spectroscopic techniques such as elemental analysis, FTIR, UV-Vis, CV, DPV and DFT calculations. In all complexes, the V(V) center is coordinated vanadium metal is pentacoordinate by two oxido groups and monoanionic tridentate ONO Schiff base ligand. The structure of the H_2L ligand and complex **1** and **2** were determined by single crystal X-ray diffraction. The FTIR spectral data showed that the ligand is coordinated with the metal center through the imino nitrogen, the phenoxo, the hydrazino

and the methoxy oxygen atoms. The electronic spectral show bands due to the ligand and the MLCT for all complexes. Room temperature magnetic susceptibility measurement indicated that the complexes are diamagnetic. In the UV-Visible spectrophotometry d-d bands are not shown in present complexes, due to $3d^0$ configuration. In-vitro α-glucosidase inhibition activity and α-amylase inhibition activity results proved that these complexes are promising anti-diabetic agents.

References

1 C.B. Aakeroy, N.R. Champness, C. Janiak, Cryst. Eng. Comm. 12 (2010) 22–43.
2 M.G. Goesten, F. Kapteijn, J. Gascon, Cryst. Eng. Comm. 15 (2013) 9249–9257.
3 M.D. Ward, P.R. Raithby, Chem. Soc. Rev. 42 (2013) 1619–1636.
4 M.W. Hosseini, Coord. Chem. Rev. 240 (2003) 157–166.
5 M.M. Safont-Sempere, G. Fernandez, F. Wurthner, Chem. Rev. 111 (2011) 5784–5814.
6 K. Biradha, C.Y. Su, J.J. Vittal, Cryst. Growth Des. 11 (2011) 875–886.
7 E.R. Parnham, R.E. Morris, Acc. Chem. Res. 40 (2007) 1005–1013.
8 G. Ferey, Chem. Soc. Rev. 37 (2007) 191–214.
9 J. Liu, L. Chen, H. Cui, J. Zhang, L. Zhang, C.Y. Su, Chem. Soc. Rev. 43 (2014) 6011–6061.
10 A. Dhakshinamoorthy, H. Garcia, Chem. Soc. Rev. 43 (2014) 5750–5765.
11 J. Lee, O. K. Farha, J. Roberts, K.A. Scheidt, S. T. Nguyen and J. T. Hupp, Chem. Soc. Rev. 38 (2009) 1450–1459.
12 B.V.D. Voorde, B. Bueken, J. Denayer, D. D. Vos, Chem. Soc. Rev. 43 (2014) 5766–5788.
13 E. Barea, C. Montoro, J.A.R. Navarro, Chem. Soc. Rev. 43 (2014) 5419–5430.
14 J.R. Li, J. Sculley, H.C. Zhou, Chem. Rev. 112 (2012) 869–932.
15 Y. He, W. Zhou, G. Qian, B. Chen, Chem. Soc. Rev. 43 (2014) 5657–5678.
16 M.P. Suh, H.J. Park, T.K. Prasad, D.-W. Lim, Chem. Rev. 112 (2012) 782–835.
17 K. Sumida, D.L. Rogow, J.A. Mason, T.M. McDonald, E.D. Bloch, Z.R. Herm, T.-H. Bae, J.R. Long, Chem. Rev. 112 (2012) 724–781.
18 Z. Hu, B.J. Deibert, J. Li, Chem. Soc. Rev. 43 (2014) 5815–5840.
19 Y. Cui, Y. Yue, G. Qian, B. Chen, Chem. Rev. 112 (2012) 1126–1162.
20 L.E. Kreno, K. Leong, O.K. Farha, M. Allendorf, R.P. Van Duyne, J.T. Hupp, Chem. Rev. 112 (2012) 1105–1125.
21 W. Zhang, R.-G. Xiong, Chem. Rev. 112 (2012) 1163–1195.
22 M. Kurmoo, Chem. Soc. Rev. 38 (2009) 1353–1379.
23 S.S. Sunkari, B. Kharediya, S. Saha, B. Elrezcd, J.P. Sutter, New J. Chem. 38 (2014) 3529–3539.
24 J. Chen, S.-H. Wang, Z.-F. Liu, M.-F. Wu, Y. Xiao, F.-K. Zheng, G.-C. Guo, J.-S. Huang, New J. Chem. 38 (2014) 269–276.

25 X.-M. Lin, H.-C. Fang, Z.-Y. Zhou, L. Chen, J.-W. Zhao, S.-Z. Zhu, Y.-P. Cai, Cryst. Eng. Comm. 11 (2009) 847–854.
26 S. Macksasitorn, Y. Hu, J. R. Stork, Cryst. Eng. Comm, 15 (2013) 1698–1705.
27 F. Jin, H.Z. Wang, Y. Zhang, Y. Wang, J. Zhang, L. Kong, F.Y. Hao, J.X. Yang, J.Y. Wu, Y.P. Tian, H.P. Zhou, Cryst. Eng. Comm. 15 (2013) 3687–3695.
28 C.-Q. Wan, A.M. Li, S.A.A. Thabaiti, T.C.W. Mak, Cryst. Growth Des. 13 (2013) 1926–1936.
29 Bruker, SMART (Version 5.631), SAINT (Version 6.45) and SADABS (Version 2.05), Bruker AXS Inc., Madison, Wisconsin, USA (2003).
30 G.M. Sheldrick, SHELXS97, SHELXL97, University of Gottingen, Germany (1997).
31 A.L. Spek, PLATON for Windows. September (1999) Version, University of Utrecht, Netherlands (1999).
32 M. Nardelli, J. Appl. Crystallogr. 28 (1995) 659.
33 C. Datta, D. Das, P. Mondal, B. Chakraborty, M. Sengupta, C.R. Bhattacharjee, Eur. J. Med. Chem. 97 (2015) 214-224.
34 S.K. Patel, R.N. Patel, Y. Singh, Y.P. Singh, D. Kumhar, R.N. Jadeja, H. Roy, A.K. Patel, N. Patel, N. Patel, A. Banerjee, D. Choquesillo-Lazarte and A. Gutierrez, Polyhedron 161 (2019) 198–212.
35 P. Sudha, S.Z. Smita, Y.B. Shobha, R.K. Ameeta, BMC Complement. Altern. Mod. 11 (2011) 5.
36 S. Al-Zuhair, A. Dowaidar, H. Kamal, J. Biochem. Tech. 2 (2010) 158-160.
37 M.J. Frisch, G.W. Trucks, H.B. Schlegel, G.E. Scuseria, M.A. Robb, J.R. Cheeseman, G. Scalmani, V. Barone, B. Mennucci, G.A. Petersson, H. Nakatsuji, M. Caricato, X. Li, H.P. Hratchian, A.F. Izmaylov, J. Bloino, G. Zheng, J.L. Sonnenberg, M. Hada, M. Ehara, K. Toyota, R. Fukuda, J. Hasegawa, M. Ishida, T. Nakajima, Y. Honda, O. Kitao, H. Nakai, T. Vreven, J.A. Montgomery Jr., J.E. Peralta, F. Ogliaro, M. Bearpark, J.J. Heyd, E. Brothers, K.N. Kudin, V.N. Staroverov, T. Keith, R. Kobayashi, J. Normand, K. Raghavachari, A. Rendell, J.C. Burant, S.S. Iyengar, J. Tomasi, M. Cossi, N. Rega, J.M. Millam, M. Klene, J.E. Knox, J.B. Cross, V. Bakken, C. Adamo, J. Jaramillo, R. Gomperts, R.E. Stratmann, O. Yazyev, A.J. Austin, R. Cammi, C. Pomelli, J.W. Ochterski, R.L. Martin, K. Morokuma, V.G. Zakrzewski, G.A. Voth, P. Salvador, J.J. Dannenberg, S. Dapprich, A.D. Daniels, O. Farkas, J.B. Foresman, J.V. Ortiz, J. Cioslowski, D.J. Fox, Gaussian 09, Revision D.01, Gaussian, Inc., Wallingford, CT, 2013.
38 P.J. Hay, W.R. Wadt, J. Chem. Phys. 82 (1985) 299-310.
39 P.J. Hay, W.R. Wadt, J. Chem. Phys. 82 (1985) 284-298.
40 P.J. Hay, W.R. Wadt, J. Chem. Phys. 82 (1985) 270-283.
41 Gauss View 5.0.9 (Gaussian Inc., Wallingford, CT, USA) (2009).
42 A.E. Reed, R.B. Weinstock, F. Weinhold, J. Phys. Chem. 83 (1985) 735–746.
43 R. Bauernschmitt, R. Ahlrichs, Chem. Phys. Lett. 256 (1996) 454–464.
44 V. Barone, M. Cossi, J. Phys. Chem. 102 (1998) 1995–2001.
45 Y.L. Sang, X.H. Zhang, X.S. Lin, Y.H. Liu, X.Y. Liu, J. Coord. Chem. 72 (2019) 3144-3155.

46 K.E. Kover, J. Borbely, Magnetic Resonance in Chemistry 23 (1985) 90-93.
47 W.J. Geary, Coord. Chem. Rev. 7 (1971)81-122.
48 I. Syiemlieh, M. Asthma, S.D. Kurhah, R.A. Lal, Polyhedron 170 (2019) 202-216.
49 W. Kemp, Organic Spectroscopy, McMillan, Hampshire, 1987. P.19.
50 M.R. Maurya, A.A. Khan, A. Azam, S. Ranjan, N. Mondal, A. Kumar, F. Avecillae, J.C. Pessoa, Dalton Trans. 39 (2010) 1345-1360.
51 N.R. Sangeetha, V. Kavita, S. Wocadlo, A.K. Powell, S. Pal, J. Coord. Chem. 51 (2000) 55-66.
52 N.R. Sangeetha, S. Pal, Bull. Chem. Soc. Jpn. 73 (2000) 357-363.
53 S.N. Pal, S. Pal, J. Chem. Crystallogr. 30 (2000) 329-333.
54 S.N. Pal, S. Pal, Acta Crystallogr., Sect. C 57 (2001) 141-142.
55 S.N. Pal, K.R. Rahika, S. Pal, Z. Anorg. Allg. Chem. 627 (2001) 1631-1637.
56 X. Li, M.S. Lah, V.L. Pecoraro, Inorg. Chem. 27 (1988) 4657-4664.
57 X.M. Zhang, X.Z. You, X. Wang, Polyhedron 15 (1996) 1793-1796.
58 A.G.J. Ligtenbarg, A.L. Spek, R. Hage, B.L. Feringa, J. Chem. Soc., Dalton Trans. (1999) 659-661.
59 M.R. Maurya, S. Khurana, C. Schulzke, D. Rehder, Eur. J. Inorg. Chem. (2001) 779-788.
60 S.Y. Ebrahimipour, J.T. Mague, A. Akbari, R. Takjoo, J. Mol. Struct. 1028 (2012) 148-155.
61 S.D. Kurbah, A. Kumar, I. Syiemlieh, R.A. Lal, Polyhedron 139 (2018) 80-88.
62 S. Orechio, V. Romano, R. Zingales, J. Chem. Res. 1 (1989) 14.
63 K. Nakamoto, Infrared and Raman Spectra of Inorganic and Coordination Compounds fifth ed., Wiley, New York, 1997.
64 M.J. Clague, N.L. Keder, A. Butler, Inorg. Chem. 32 (1993) 4754-4761.
65 C.J. Carrano, M. Mohan, S.M. Holmes, R.D.L. Rosa, A. Butler, J.M. Charnock, C.D. Garner, Inorg. Chem. 33 (1994) 646-655.
66 J.M. Arber, E.D. Boer, C.D. Garner, S.S. Hasnain, R. Wever, Biochemistry 28 (1989) 7968-7973.
67 X. Li , M.S. Lah, V.L. Pecoraro, Inorg. Chem. 27 (1988) 4657-4664.
68 A.G.J. Ligtenbarg, A.L. Spek, R. Hage, B.L. Feringa, J. Chem. Soc. Dalton Trans. 5 (1999) 659-662.
69 S.Y. Ebrahimipour, M. Abaszadeh, J. Castro, M. Seifi, Polyhedron 79 (2014) 138-150.
70 R.N. Patel, Y.P. Singh, Y. Singh, R.J. Butcher, J.P. Jasinski, Polyhedron 133 (2017) 102-109.
71 S. Samanta, D. Ghosh, S. Mukhopadhyay, A. Endo, T.J.R. Weakley, M. Chaudhury, Inorg. Chem. 42 (2003)1508-1517.
72 H. Sakurai, Y. Yoshikawa, H. Yasui, Chem. Soc. Rev. 37 (2008)2383-2392.
73 D. Rehder, J.C. Pessoa, C.F. Geraldes, M.M. Castro, T. Kabanos, T. Kiss, B. Meier, G. Micera, L. Pettersson, M. Rngel, A. Salifoglou, I. Turel, D. Wang, J. Biol. Inorg. Chem. 7 (2002)384-396.
74 H. Michibata, Vanadium: Biochemical, Molecular Biological Approaches, Springer, Netherlands, (2011).

75 S.J. Park, C.K. Youn, J.W. Hyun, H.J. You, Biol. Trace. Elem. Res. 151 (2013) 294-300.

76 B. Mukherjee, B. Patra, S. Mahapatra, P. Banerjee, A. Tiwari, M. Chatterjee, Toxicol. Lett. 150 (2004) 135-143.

77 A.M. Evangelou, Crit. Rev. Oncol. Hematol. 42 (2002) 249-265.

78 A. Bishayee, A. Waghray, M.A. Patel, M. Chatterjee, Cancer Lett. 294 (2010) 1-12.

79 S. Kumar, M. Munjal, J. Singh, R. Gupta, Eur. J. Inorg. Chem. 29 (2014) 4957-4965.

80 S. Kumar, R. Gupta, Eur. J. Inorg. Chem. 32 (2014) 5567-5576.

81 S. Kumar, S. Vaidya, M. Pissas, Y. Sanakis, R. Gupta, Eur. J. Inorg. Chem. 33 (2012) 5525-5533.

82 S. Kumar, R.R. Jha, S. Yadav, R. Gupta, New J. Chem. 39 (2015) 2042-2051.

83 M.J. Rose, P.K. Mascharak, Coord. Chem. Rev. 252 (2008) 2093-2114.

84 A. Rajput, R. Mukherjee, Coord. Chem. Rev. 257 (2013) 350-368.

85 D.S. Marlin, P.K. Mascharak, Chem. Soc. Rev. 29 (2000) 69-74.

86 S.P. Dash, S. Majumder, A. Banerjee, M.F.N.N. Carvalho, P. Adao, J.C. Pessoa, K. Brzezinski, E. Garribba, H. Reuter, R. Dinda, Inorg. Chem. 55 (2016) 1165-1182.

87 A.W. Addison, T.N. Rao, J. Reedijk, J.V. Rijn, G.C. Verschoor, J. Chem. Soc. Dalton Trans. (1984) 1349-1356.

88 S.Y. Ebrahimipour, M. Abaszadeh, J. Castro, M. Seifi, Polyhedron 79 (2014) 138-150.

89 Z. Qin, M.C. Jennings, R.J. Puddephatt, Eur. J. Inorg. Chem. 42 (2003) 1956-1965.

90 A. Bayler, A. Bauer, H. Schmidbaur, Chem. Ber. 130 (1997) 115-118.

91 S. Das, Polyhedron 27 (2008) 517-522.

92 S.Y. Ebrahimipour, J.T. Mague, A. Akbari, R. Takjoo, J. Mol. Struct. 1028 (2012) 148-155.

93 V.K. Muppidi, P.S. Zacharias, S. Pal, Chem. Commun. (2005) 2515-2517.

94 X. Wei, X. Du, D. Chen, Z. Chen, Thermochim. Acta 440 (2006) 181-187.

95 S.Y. Ebrahiipour, J.T. Mague, A. Akbari, R. Takjoo, J. Mol. Struct. 1028 (2012) 148-155.

96 S.S. Wazalwar, N.S. Bhave, Synth. React. Inorg. Met. Org. 42 (2012) 1098-1104.

97 R. Amarowicz, R.B. Pegg, P.R. Moghaddam, B. Barl, J.A. Weil, Food Chem. 84 (2004) 551-562.

98 S. Andotra, S. Kumar, M. Kour, Vikas, Chayawan, V. Sharma, S. Jaglan, S.K. Pandey, Spectrochim. Acta Part A 180 (2017) 127-137.

99 Y. Singh, R.N. Patel, S.K. Patel, A.K. Patel, N. Patel, R. Singh, R.J. Butcher, J.P. Jasinski, A. Gutierrez, Polyhedron 171 (2019) 155–171.

100 R.N. Patel, Y. Singh, Y.P. Singh, A.K. Patel, N. Patel, R. Singh, R.J. Butcher, J.P. Jasinski, E. Colacio, M.A. Palacios, New J. Chem. 42 (2018) 3112-3136.

101 N. Patel, A. K. Prajapati, R.N. Jadeja, R.N Patel, S.K. Patel, V. K. Gupta, I. P. Tripathi, N. Dwivedi. Inorg. Chem. Acta 493 (2019) 20-28.

102 S. Zhang, S.M. Kim, Appl. Organomet. Chem. (2019) 1-12.

103 I.P. Tripathi, A. Kamal, M.K. Mishra, A. Dwivedi, R. Tripathi, C. Mishra, L. Shastri, Ind. J. Appl. Res. 4 (2014) 66-69.

104 M.K. Bhat, B.S. Chadha, B.A. Kumar, G.S. Kaur, J. Gen. Microbiol. 139 (1993) 2825-2832.

105 S. Misra, K.B. Pandey, A.K. Tiwari, A.Z. Ali, T. Saradamani, S.B. Agawane, K. Madhusudana, Int. J. Nutr. Metab. 4 (2012) 11-18.
106 Apostolidis, Y.I.I. Kwon, K. Shetty, Asian Pac. J. Clin. Nutr. 15 (2006) 433-441.
107 S. Zhang, S.M. Kim, Appl. Organomet. Chem. 33 (2019) e5102.
108 J. Xio, X. Ni, G. Kai, X. Chem, Critical Reviews in Food Science and Nutrition 53 (2013) 497-506.
109 M.A. Spackman, J.J. McKinnon, Cryst. Eng. Comm. 4 (2002) 378-392.
110 M.A. Spackman, P.G. Byrom, Chem. Phy. Lett. 267 (1997) 309.
111 J.J. McKinnon, A.S. Mitchell, M.A. Spackman, J. Eur. Chem. 4 (1998) 2136-2141.
112 J.J. McKinnon, M.A. Spackman, A.S. Mitchell, Acta Crystallogr. Sec. B 60 (2004) 627 668.
113 A.L. Rohl, M. Moret, W. Kaminsky, K. Claborn, J.J. McKinnon, B. Kahr, Cryst. Growth Des. 8 (2008) 4517-4525
114 A. Parkin, G. Barr, W. Dong, C.J. Gilmore, D. Jayatilaka, J.J. McKinnon, M.A. Spackman, C.C. Wilson, Cryst. Eng. Comm. 9 (2008) 648-652.
115 S.K. Wolff, D.J. Greenwood, J.J. McKinnon, D. Jayatilaka, M.A. Spackman, Crystal Explorer 2.0; University of Western Australia: Perth, Australia, (2007).
116 J.J. Koenderink, A.J.V. Doorn, Image Vision Comput.10 (1992) 557-564.
117 R.S. Mulliken, J. Chem. Phy. 23 (1955) 1833-1840.
118 V. Balachandran, K. Parimala, Spectrochim. Acta, A 96 (2012) 340-351.
119 A. Lakshmi, V. Balachandran, J. Mol. Struct. 1033 (2013) 40-50.
120 C.J. Carrano, M. Mohan, S.M. Holmes, R.D.L. Rosa, A. Butler, J.M. Charnock, C.D. Garner, Inorg. Chem. 33 (1994) 646-655.
121 J.M. Arber, E.D. Boer, C.D. Garner, S.S. Hasnain, R. Wever, Biochemistry 28 (1989) 7968-7973.
122 X. Li , M.S. Lah, V.L. Pecoraro, Inorg. Chem. 27 (1988) 4657-4664.
123 A.G.J. Ligtenbarg, A.L. Spek, R. Hage, B.L. Feringa, J. Chem. Soc. Dalton Trans. 5 (1999) 659-662.
124 S.Y. Ebrahimipour, M. Abaszadeh, J. Castro, M. Seifi, Polyhedron 79 (2014) 138-150.
125 R.N. Patel, Y.P. Singh, Y. Singh, R.J. Butcher, J.P. Jasinski, Polyhedron 133 (2017) 102-109.
126 S. Samanta, D. Ghosh, S. Mukhopadhyay, A. Endo, T.J.R. Weakley, M. Chaudhury, Inorg. Chem. 42 (2003)1508-1517.
127 H. Sakurai, Y. Yoshikawa, H. Yasui, Chem. Soc. Rev. 37 (2008) 2383-2392.
128 D. Rehder, J.C. Pessoa, C.F. Geraldes, M.M. Castro, T. Kabanos, T. Kiss, B. Meier, G. Micera, L. Pettersson, M. Rngel, A. Salifoglou, I. Turel, D. Wang, J. Biol. Inorg. Chem. 7 (2002) 384-396
129 H. Michibata, Vanadium: Biochemical, Molecular Biological Approaches, Springer, Netherlands (2011).
130 S.J. Park, C.K. Youn, J.W. Hyun, H.J. You, Biol. Trace. Elem. Res. 151 (2013) 294-300.

Paper Published from this Chapter

Polyhedron 180 (2020) 114434

Contents lists available at ScienceDirect

Polyhedron

journal homepage: www.elsevier.com/locate/poly

Dioxidovanadium(V) complexes of a tridentate ONO Schiff base ligand: Structural characterization, quantum chemical calculations and *in-vitro* antidiabetic activity

Neetu Patel [a], A.K. Prajapati [a], R.N. Jadeja [a,*], R.N. Patel [b], S.K. Patel [b], I.P. Tripathi [c], N. Dwivedi [c], V.K. Gupta [d], Raymond.J. Butcher [e]

[a] Department of Chemistry, Faculty of Science, The Maharaja Sayajirao University of Baroda, Vadodara 390002, India
[b] Department of Chemistry, A.P.S. University, Rewa, M.P 486003, India
[c] Department of Chemistry, MGCGV, Chitrakoot, Satna, M.P 485334, India
[d] Department of Physics, University of Jammu, Jammu Tawi 180006, India
[e] Department of Inorganic & Structural Chemistry, Howard University, Washington, DC 22031, USA

ARTICLE INFO

Article history:
Received 16 January 2020
Accepted 9 February 2020
Available online 11 February 2020

Keywords:
Dioxidovanadium(V) complexes
Crystal structures
UV–vis
Computational study
Antidiabetic activity

ABSTRACT

Two new dioxidovanadium(V) complexes $[V(O)_2(L)]$Him **1** and $[V(O)_2(L)]$H2Meim **2**, incorporating tridentate ligand Nicotinic acid (2-hydroxy-3-methoxy-benzylidene)-hydrazide (H_2L) and imidazoles (Him = imidazole and H2Meim = methylimidazole) was substantiated. The crystal structures of both complexes were solved by single-crystal X-ray analysis. In both complexes, the V(V) center is coordinated by ONO donar set of L^{2-} ligand and two oxido groups in a distorted square pyramidal geometry. UV–visible spectra, infrared spectra and electrochemical properties of both complexes were also reported. Room temperature magnetic susceptibility was performed to disclose the diamagnetic nature of complexes **1** and **2**. The quantum chemical calculations authenticated the molecular structures and reactivity of the complexes. Antidiabetic activities of the complexes have also been investigated. An antidiabetic feature like α-amylase and α-glucosidase inhibition studies made them promising agents as inhibitors of insulin enzyme.